



PCCP

A systematic model study quantifying how conical intersection topography modulates photochemical reactions

Journal:	<i>Physical Chemistry Chemical Physics</i>
Manuscript ID	CP-ART-06-2020-003464.R1
Article Type:	Paper
Date Submitted by the Author:	26-Aug-2020
Complete List of Authors:	Farfan, Camille; New York University School of Arts and Science, Chemistry Turner, Daniel; Boise State University College of Education, Materials Science and Engineering

SCHOLARONE™
Manuscripts

Cite this: DOI: 00.0000/xxxxxxxxxx

A systematic model study quantifying how conical intersection topography modulates photochemical reactions

Camille A. Farfan^a and Daniel B. Turner^{*ab}

Received Date

Accepted Date

DOI: 00.0000/xxxxxxxxxx

Despite their important role in photochemistry and expected presence in most polyatomic molecules, conical intersections have been thoroughly characterized in a comparatively small number of systems. Conical intersections can confer molecular photoreactivity or photostability, often with remarkable efficacy, due to their unique structure: At a conical intersection, the adiabatic potential energy surfaces of two or more electronic states are degenerate, enabling ultrafast decay from an excited state without radiative emission, known as nonadiabatic transfer. Furthermore, the precise conical intersection topography determines fundamental properties of photochemical processes, including excited-state decay rate, efficacy, and molecular products that are formed. However, these relationships have yet to be defined comprehensively. In this article, we use an adaptable computational model to investigate a variety of conical intersection topographies, simulate resulting nonadiabatic dynamics, and calculate key photochemical observables. We varied the vibrational mode frequencies to modify conical intersection topography systematically in four primary classes of conical intersections and quantified the resulting rate, total yield, and product yield of nonadiabatic decay. The results reveal that higher vibrational mode frequencies reduce nonadiabatic transfer, but increase the transfer rate and resulting photoproduct formation. These trends can inform progress toward experimental control of photochemical reactions or tuning of molecules' photochemical properties based on conical intersections and their topography.

1 Introduction

Conical intersections dramatically influence photochemical processes because they promote extremely rapid, ultrafast decay that takes place without the emission of radiation, through the process of nonadiabatic transfer. The presence of a conical intersection can confer a molecule with notable photochemical properties such as a remarkably high photoproduct yield or unexpectedly negligible fluorescence, which are two of the most recognizable manifestations of a conical intersection's influence.¹ A conical intersection occurs when potential energy surfaces of different electronic states are degenerate, and theoretical studies have concluded that this is very likely to occur in nearly all polyatomic molecules.^{2–5} However, the unique quantum properties of conical intersections, and the extremely rapid dynamic effects they induce, have presented a challenge for both *ab initio* quantum-chemical simulations and laboratory experiments.^{6–8} As a result, the number of molecules in which conical intersections have been detected experimentally or calculated computationally remains relatively small compared to their expected ubiquity.

Conical intersections are an influential feature of adiabatic potential energy surfaces representing the electronic states of a molecule.^{1,9,10} The potential energy surface landscape determines the rate and trajectory of excited-state processes, which can be observed as the evolution of a coherent vibrational wavepacket across the surface.^{11–14} Many reduced-dimension computational models have been developed for these purposes, and continue to prove useful and convenient in studying fundamental aspects of nonadiabatic processes.^{15–23} Furthermore, the specific topography of the conical intersection is a major determinant of the nonadiabatic transfer dynamics. Foundational model studies have thoroughly demonstrated the fundamental influence of topography on nonadiabatic transfer and the wavepacket dynamics involved.^{24–28} In addition to static features of the potential energy surfaces, examination of dynamics is also critical to determine the outcomes of nonadiabatic processes accurately.^{5,26,29} The direction and velocity of the wavepacket's approach to the conical intersection,²⁸ the energetic accessibility of the conical intersection for wavepacket dynamics,³⁰ and the extent of wavepacket delocalization²⁷ and coherence^{31,32} are all factors that influence the rate and results of nonadiabatic transfer.

The conical intersection topography and resulting nonadiabatic dynamics also determine the overall photochemistry of

^a Department of Chemistry, New York University, New York, NY 10003, USA

^b Present address: Micron School of Materials Science and Engineering, Boise State University, Boise, ID 83725, USA. Email: danielturner926@boisestate.edu

a molecule.¹⁰ Computational quantum dynamics studies^{9,33–37} and spectroscopic measurements^{5,38,39} on a number of compounds have demonstrated how conical intersection topography in particular determines the pathways of photochemical reactions and excited-state relaxation, as well as the product yields and fluorescence properties specific to a molecule. The important connection between nonadiabatic wavepacket dynamics on the quantum scale and photochemical behavior on the molecular scale has been illustrated in notable studies that have applied information on the potential energy surface topography to rationalize experimental observations, and vice versa.^{40–42}

Despite the wealth of critical knowledge gained from previous studies, a comprehensive description of how chemical modifications alter potential energy surface and conical intersection topography, how topographical changes modulate nonadiabatic dynamics, and how the process of nonadiabatic wavepacket transfer corresponds to molecular photochemistry has not been fully defined. Furthermore, our existing knowledge of conical intersections in photochemistry still needs to be expanded beyond specific well-known examples to achieve more comprehensive understanding and facilitate use in related fields and applications. This could enable rational design of molecules with different functional properties such as photostability or photoreactivity,^{36,43,44} optimization of reaction rates or excited-state lifetimes,^{45–47} formation of different products,^{48–50} and even direct experimental control over photochemistry,^{43,49,51,52} by utilizing conical intersections and their topography in the future.

In this article, we refine relationships between the conical intersection topography, nonadiabatic dynamics, and reaction outcomes by assessing critical photochemical observables: the time duration and total extent of nonadiabatic transfer, and the photoproduct yield. We aim to elucidate overall trends that will be applicable to specific, more complex molecular systems and useful for interpreting the effects of conical intersections throughout other studies. To accomplish this, we used an adaptable and efficient computational model to investigate a wide range of conical intersection topographies and simulate the resulting wavepacket dynamics under the influence of nonadiabatic effects. First, we introduce four main classifications of conical intersection topographies that we use to organize this work, displaying model examples and discussing their roles in photochemical processes. Then, for each type, we demonstrate how manipulation of a molecule's vibrational mode frequencies affects the potential energy surface topography and ultimately modulates the rate and efficacy of nonadiabatic transfer, as well as the resulting distribution of molecular products. We discuss the overall trends in these relationships, provide detailed rationale based on the wavepacket dynamics, and elaborate on some specific dynamic behaviors.

2 Conical Intersection Topographies in Photochemistry

Conical intersection topographies are conventionally categorized as *peaked* (Fig. 1a) or *sloped* (Fig. 1b). In this study, we use their established quantitative definitions.^{53,54} In addition, here we distinguish between conical intersections with *one path* or *two*

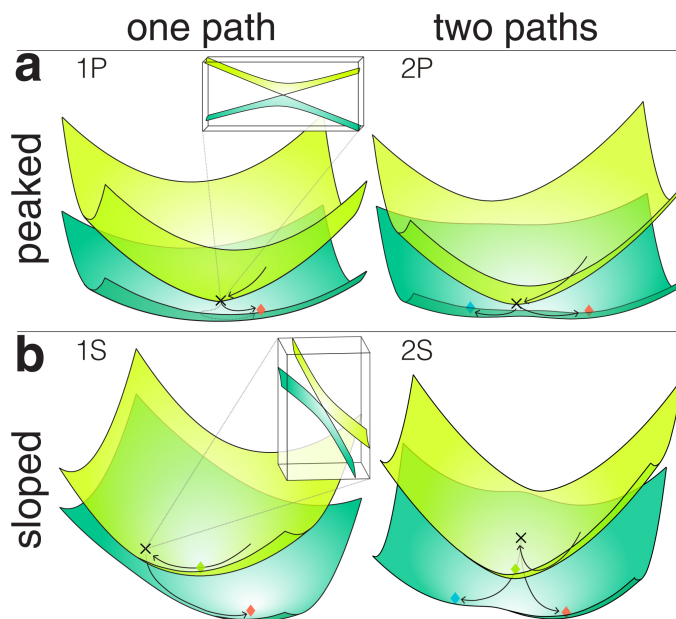


Fig. 1 Four types of conical intersections: (a) *peaked* or (b) *sloped* topography, leading to *one path* (left panels) or *two paths* (right panels) on the ground state. The ground state and excited state adiabatic potential energy surfaces are degenerate at the conical intersection (x). The conical intersection location coincides with the excited-state minimum in *peaked* topographies (a), but is displaced from the excited-state minimum (★) in *sloped* topographies (b). Transfer through the intersection leads to regeneration of the reactant species (♦) if there is *one path*, or can also lead to formation of a new photoproduct (◆) if there are *two paths*. Arrows illustrate the primary paths in each model, and insets in the left panels show a larger view of the conical intersection region.

paths (i.e. “single path” or “bifurcating”) based on the comprehensive and systematic characterization methodology developed by Galván, *et al.*⁵⁴ These terms refer to the number of molecular pathways that can be accessed via nonadiabatic transfer to the ground state. In total, we examine four primary types of conical intersection topography, which are modeled in Fig. 1: peaked with one path – 1P, sloped with one path – 1S, peaked with two paths – 2P, and sloped with two paths – 2S.

The number of pathways accessible through a conical intersection is a simple yet fundamental property: Having one path indicates that nonadiabatic decay directs the molecule entirely toward the formation of a single molecular species, the initial reactant, meaning the ground-state reactant species is regenerated after excitation (Fig. 1, left panels). Therefore conical intersection topographies that funnel trajectories toward a single pathway are fundamental in molecules exhibiting photostability. This pathway is unproductive in terms of product formation, but serves a critical function in many molecules—often biochemical compounds, such as the nucleotides in DNA.^{55,56} In contrast, having two paths indicates that nonadiabatic transfer can form two possible molecular species, usually either regenerating the reactant or forming a new photoproduct (Fig. 1, right panels). This category is therefore responsible for photochemical reactions, with one of the most famous examples being *cis-trans* photoisomerization in the retinal chromophore of rhodopsin.^{57–59} Conical intersections can lead to multiple pathways toward several different

products, which is well-known in benzene,^{60,61} dienes such as butadiene⁶² and cyclohexadiene,⁶³ and compounds with similar structural motifs like fulgides.⁶⁴ However, here we focus on the formation of one primary product through reactions in bound states, which is a common scenario in many molecules including benzene—although alternative pathways exist, they are unfavorable enough that these products are not observed in nature.

In a peaked conical intersection (Fig. 1a), the intersection point is located at the effective minimum of the excited-state potential energy surface. The topography usually has a low tilt angle and tends toward higher symmetry. Peaked conical intersections form the canonical “photochemical funnel” feature that is highly efficient for nonadiabatic transfer and photoproduct formation.^{9,10,40,65} This efficiency results from the dynamic effects of the topography, which funnels the wavepacket directly toward the energetically-favorable conical intersection after excitation. In addition, peaked topographies often facilitate transfer of a large or complete portion of the wavepacket population to the lower potential energy surface in the first passage through the conical intersection, keeping the wavepacket largely intact with minimal splitting and fragmentation,^{24,27} as illustrated in Fig. 2a.

A great enough tilt (often enhanced by asymmetry) produces a sloped conical intersection (Fig. 1b) in which the conical intersection location does not coincide with the excited-state minimum, so it does not form the apex of the upper surface funnel as in peaked topographies.^{3,24,54} Therefore the conical intersection is displaced and higher in energy than the favorable minimum, requiring some extent of uphill motion to be accessed by the wavepacket. As a result, sloped topographies tend to induce gradual or incremental nonadiabatic transfer of smaller wavepacket fractions (Fig. 2b), requiring the wavepacket to cross over the conical intersection point multiple times.^{26,27} Typically these topographies have a steep gradient leading from the intersection point in one direction on the lower potential energy surface. This confers more momentum to the wavepacket after it is transferred to the lower state, which increases the probability of reverse wavepacket transfer back to the upper state and further contributes to the incremental nature of the transfer dynamics.^{12,34} Nonetheless, the stepwise transfer dynamics induced by sloped topographies do not imply that they always require longer timescales than peaked intersections, nor that they are inherently less probable for nonadiabatic transfer.²⁸ Lastly, conical intersections also span the entire range from peaked to sloped: slightly sloped or slightly peaked topographies, as well as intermediate topographies, are possible.

In addition, peaked and sloped topographies typically serve different roles in photochemistry. Peaked conical intersections are most often responsible for photoreactions—including isomerization, dissociation, cyclization, and charge transfer—and can promote rapid product formation with high photochemical quantum yields. Thus peaked topographies often lead to *two paths* (or more) on the ground state. Examples include photoisomerization in the rhodopsin chromophore^{34,58,66} and photochromic molecules such as azomethane^{67,68} and azobenzene derivatives,^{69,70} which have demonstrated timescales of roughly 150 fs or less and photochemical quantum yields of 0.6–0.7.

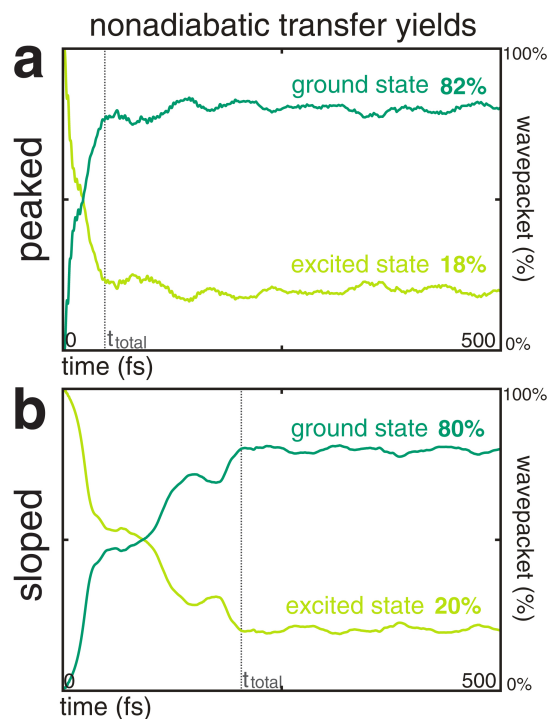


Fig. 2 Examples of *nonadiabatic transfer yields* over time from dynamics simulations in (a) *peaked* and (b) *sloped* conical intersection models. Plots show the percentage of the total wavepacket population on the adiabatic **ground state** and **excited state** during initial dynamics from 0–500 fs. Dotted lines mark the time at which the extent of nonadiabatic transfer begins to stabilize close to the average final value (t_{total}).

(While rhodopsin is the canonical example of a peaked conical intersection, there are in fact many animal and microbial variants within the vast rhodopsin protein family, which are also known to vary in energetic landscape around the conical intersection—including topography, relaxation pathways, potential barriers, and isomerization mechanisms.^{71,72}) In contrast, photostability is most often conferred by sloped conical intersections. Sloped intersections commonly occur when the excited- and ground-state molecular conformations are similar, leading to *one path* on the ground state that re-forms the reactant. Well-known examples include anomalous fluorescence from the S_2 state in azulene,^{73,74} short fluorescence lifetimes in cyanine dyes,³³ and photostability in DNA/RNA nucleobases and their derivatives.^{75–78}

Of course, conical intersection topographies are not limited to the most common roles just described. Some photoreactions take place through sloped intersections, but fewer examples have been identified so far. Overall, although the number of conical intersections that have been observed in real molecules remains a small sample size compared to their expected commonplace occurrence, known examples generally fit the roles discussed above.⁵⁴ Especially in less common types of conical intersections, the sensitivity of key photochemical properties to topographical parameters has not yet been comprehensively determined. To investigate and refine these relationships in different types of conical intersections, we use an adaptable model to tune conical intersection topography and simulate the resulting nonadiabatic dynamics.

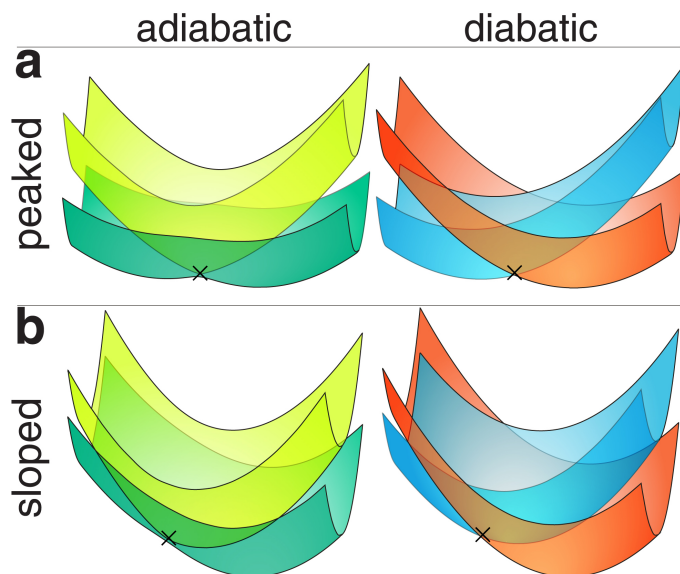


Fig. 3 Example potential energy surface models for (a) *peaked* and (b) *sloped* conical intersection topographies, displayed in the *adiabatic* representation (left panels) and the *diabatic* representation (right panels). The conical intersection location is labeled with \times . The adiabatic representation preserves the energy levels of the electronic state surfaces so that they can be distinguished as the *ground state* and *excited state*. The diabatic representation preserves the distinct chemical identity of the surfaces so they can be distinguished as the *reactant* and *product* species (or *excited intermediate*, as shown in *b*).

3 Computational methods

A wide array of methods are available for both electronic structure calculations and molecular dynamics simulations.^{79–83} Such computations are greatly complicated by the presence of a conical intersection, which necessitates calculation of the nonadiabatic coupling and invalidates the Born–Oppenheimer approximation, on which the majority of quantum-chemical theory and calculation methods are based.^{7,84–88} In addition, issues unique to conical intersections such as the geometric phase effect, nonadiabatic coupling singularities, and the often highly-multidimensional nature of conical intersections must be overcome. Because these calculations are quite demanding, most studies analyze the conical intersection(s) of a single molecule in great detail, but altogether have been limited in the number of molecules studied so far.

Symmetry-induced conical intersections⁸⁹ have already been thoroughly characterized in diatomic and triatomic molecules.^{25,53,90,91} In contrast, conical intersections that are not symmetry-specific are very likely to occur in polyatomic molecules⁹² but are also more difficult to locate and assess, so it is likely that many of these conical intersections remain unexplored. Therefore this study focuses on the “accidental” conical intersections that occur in polyatomic molecules between states of the same symmetry.⁸⁹ (Thus spin and symmetry constraints are not implemented.) Unlike symmetry-induced intersections, same-symmetry conical intersections are not subject to precise topographical criteria,⁵³ allowing us to investigate a wide variety of possible topographies. But, symmetry-specified conical intersections such as Jahn–Teller intersections and photodissociation

processes fall outside the scope of this study.

We used a convenient and adaptable potential energy surface model to construct a variety of conical intersection topographies and examine how topographical changes affect wavepacket dynamics during nonadiabatic transfer. Here we describe the main features of the model, which we also detailed in ref. 30, and discuss the specifics of its implementation toward the research in the present article. Among nonadiabatic dynamics models, grid-based calculation methods are widely used for studies of fundamental properties^{15,16,93–95} as well as investigations of reactions in specific molecules.^{96–98} Here we use the discrete variable representation (DVR),^{99–101} which enables efficient calculation of the potential energy surfaces over a grid of discrete position coordinates.^{102–104} Another benefit is that computational issues arising from the nonadiabatic coupling singularity that characterizes the conical intersection point in the adiabatic representation can be avoided—by setting the grid points not to include the precise coordinates of the conical intersection, but a coordinate point extremely close by. (Due to the nature of this method, tests showed that changing the grid coordinate proximity to the conical intersection produces the same results.) In this model, DVR is extended to two dimensions to construct, and visualize, a conical intersection in the two-dimensional branching space.^{3,4,24}

While 2D models like the one presented here are immensely useful for investigating fundamental nonadiabatic properties in nonspecific contexts,^{15,16,19,20} naturally this utility has a cost—not all the nuances of more complicated nonadiabatic systems can be captured in two dimensions. As research progresses, molecules continue to be revealed in which multiple vibrational modes in addition to the branching modes, and multiple conical intersection locations along a seam of the intersection space, are involved in excited-state dynamics. For example, additional molecular vibrations can be necessary to reach the branching space of the conical intersection.^{65,72,105–108} Furthermore, it has been demonstrated that nonadiabatic decay can take place through many intersection points across a region of the seam,^{60,109–111} and that different conical intersections in a molecule can be utilized for different mechanisms.^{112–117} For these reasons, it is important to continue research efforts toward global analysis of all dimensions and all conical intersections within a molecule, not just the minimum-energy conical intersection. 2D models nevertheless cannot assess the higher dimensions of the seam space—but extension to more dimensions and vibrational modes is more relevant for specific molecular systems, and would add difficulties for preserving the general applicability of results from our model. However, development of similar models for three or more dimensions remains a worthy goal for future studies—3D models are applicable to molecules in the retinal class, and potentially others in which three modes are involved.^{118,119}

3.1 Two-dimensional potential energy surface models

In our 2D model of the conical intersection branching space, the two coordinates x and y represent the two branching coordinates. Consistent with convention, we use x to correspond to the tuning coordinate (g), and y to correspond to the coupling coordinate

(h). For conciseness in equations, we refer to both coordinates as \mathbf{R} . To use DVR, we diagonalize the harmonic oscillator position matrices \mathbf{R}_{HO} to transform them into the DVR basis, which also yields the corresponding transformation matrices:

$$\mathbf{T}_{\text{DVR}}^\dagger \mathbf{R}_{\text{HO}} \mathbf{T}_{\text{DVR}} = \mathbf{R}_{\text{DVR}}. \quad (1)$$

In the DVR basis, the position matrices are diagonal, which greatly facilitates further calculations. For all models, calculations were done using 8100 basis functions and a coordinate grid of at least 200 units in each dimension.

Within the branching space, we model two electronic states of a molecule as a two-level system of quantum harmonic oscillators. We calculate the potential energy surfaces representing the electronic states in both the *diabatic* representation, in which the two surfaces maintain distinct and defined chemical identities, and the *adiabatic* representation, in which the surfaces represent defined energy levels and remain eigenstates of the Hamiltonian but do not preserve the distinct chemical character of the system around the conical intersection.^{85,120} Therefore, as shown in Fig. 3, the adiabatic states can be distinguished as the “ground” and “excited” states, labeled g and e , and the diabatic states as the “reactant” and “product” states, labeled r and p . We will use these labels consistently throughout the article.

The two diabatic electronic potential energy surfaces (Fig. 3, right panels) are defined over the branching coordinates as

$$\begin{aligned} \hat{V}_{diab}^r(\mathbf{R}) &= \frac{1}{2} \omega_r^2 \mathbf{R}^2 \\ \hat{V}_{diab}^p(\mathbf{R}) &= \frac{1}{2} \omega_r^2 (\mathbf{R} - \mathbf{R}_0)^2 + \Delta E. \end{aligned} \quad (2)$$

The complete diabatic potential energy requires addition of the term \hat{d}_{diab} for linear coupling along the coupling coordinate \mathbf{R}_y , which is applied in only the diabatic basis with the expression

$$\hat{d}_{diab}(\mathbf{R}_y) = \mu \mathbf{R}_y + \beta. \quad (3)$$

Therefore, the input parameters for the model are the coordinate displacement (\mathbf{R}_0) and energy difference (ΔE) between the surfaces (with respect to the surface minima), the linear coupling parameters (μ , β), and the frequencies of the branching coordinates (ω_r). The complete matrix for the diabatic potential energy is then:

$$\mathbf{V}_{diab}^{r,p} = \begin{bmatrix} V_{diab}^r & d_{diab} \\ d_{diab} & V_{diab}^p \end{bmatrix}$$

Diagonalization of the diabatic potential matrix eliminates the off-diagonal elements, obtaining the potential energy in the adiabatic representation:

$$\mathbf{V}_{adia}^{g,e} = \begin{bmatrix} V_{adia}^g & 0 \\ 0 & V_{adia}^e \end{bmatrix}$$

The resulting adiabatic electronic potential energy surfaces (Fig.

3, left panels) have the expressions

$$\begin{aligned} \hat{V}_{adia}^g(\mathbf{R}) &= \frac{1}{2} (\hat{V}_{diab}^p(\mathbf{R}) + \hat{V}_{diab}^r(\mathbf{R})) \\ &\quad - \frac{1}{2} \sqrt{(\hat{V}_{diab}^p(\mathbf{R}) - \hat{V}_{diab}^r(\mathbf{R}))^2 + 4\hat{d}_{diab}(\mathbf{R}_y)^2} \\ \hat{V}_{adia}^e(\mathbf{R}) &= \frac{1}{2} (\hat{V}_{diab}^p(\mathbf{R}) + \hat{V}_{diab}^r(\mathbf{R})) \\ &\quad + \frac{1}{2} \sqrt{(\hat{V}_{diab}^p(\mathbf{R}) - \hat{V}_{diab}^r(\mathbf{R}))^2 + 4\hat{d}_{diab}(\mathbf{R}_y)^2} \end{aligned} \quad (4)$$

and are therefore dependent on the same parameters as $\hat{V}_{diab}^{r,p}$ and \hat{d}_{diab} . To evaluate both the diabatic and adiabatic potential energy surfaces above, we use \mathbf{R}_{DVR} from eqn (1) as \mathbf{R} , which makes calculations much more efficient. Then, the potential energy matrices $\mathbf{V}_{diab}^{r,p}(\mathbf{R}_{\text{DVR}})$ and $\mathbf{V}_{adia}^{g,e}(\mathbf{R}_{\text{DVR}})$ are transformed conveniently back into the harmonic oscillator basis by applying \mathbf{T}_{DVR} .

3.2 Systematic topography variations

It is already well-established that nonadiabatic behavior depends fundamentally on the interstate coupling, \mathbf{h} , and the potential energy difference, expressed by the energy difference gradient, \mathbf{g} —the two branching coordinates.⁵³ Therefore, we implemented changes in the vibrational mode frequencies that determine \mathbf{g} and \mathbf{h} to investigate how the vibrational modes—a familiar molecular property—affect the particular conical intersection topography and influence nonadiabatic dynamics. Moreover, tests that manipulated the vibrational modes in specific molecules through chemical substitution or vibrational damping variations, for example, have already established that the modes have major significance and can alter outcomes including the rate and photochemical quantum yield.^{32,106,121,122} In the model presented here, the frequency parameters ω_x and ω_y , represented by ω_r , correspond to the two vibrational modes of the molecule that allow the conical intersection to occur, and thus define the branching coordinates.¹ These branching modes are the particular molecular vibrations that allow the molecule to reach the specific atomic configuration required for the conical intersection. Specifically, v_x (ω_x) corresponds to the tuning mode, and v_y (ω_y) corresponds to the coupling mode.

In models for each class of conical intersection described above, we examined how systematic changes in topography affect the nonadiabatic transfer process and its photochemical outcomes by varying the vibrational frequencies of the branching modes, v_x and v_y , individually and in combination (labeled v_{xy}). In total, we tested three series of topography models (Δv_x , Δv_y , and Δv_{xy}) for each type of conical intersection (**1P**, **1S**, **2P**, and **2S**), as listed in Table 1. We used frequencies within a range of 4–20 THz for each series, and ensured that all topographies remained representative of their designated class. The properties defining each class also defined the limits for the range of frequencies that could be applied—with large enough changes in frequency, we found that topography can shift from peaked to sloped, or a single reaction path can bifurcate into two paths, for example. For each category, we show one best representative model. Although the po-

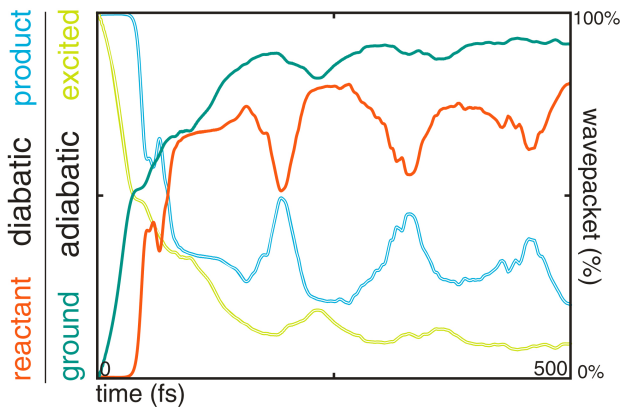


Fig. 4 Nonadiabatic transfer in the adiabatic and diabatic representations. Wavepacket populations on the adiabatic ground state and excited state differ from populations on the diabatic reactant state and product state, as expressed in eqns (9) and (11). Each representation defines the electronic states (and the conical intersection) distinctly, as shown in Fig. 3, and thus provides different information on the nonadiabatic process.

tential energy surfaces can vary widely within each category, we found the resulting trends to be consistent across other models of the same category. Lastly, to maintain the general applicability of results from these models, we exclude other molecule-specific features such as energetic barriers.

3.3 Nonadiabatic wavepacket dynamics and photochemical observables

In each topography model, we construct the complete Hamiltonian including coupling, and simulate wavepacket dynamics in both the adiabatic and diabatic representations. The Hamiltonian in each representation is

$$\begin{aligned}\widehat{H}_{adia}^{g,e}(\mathbf{R}_{HO}) &= \widehat{T}_{nuc}(\mathbf{R}_{HO}) + \widehat{V}_{adia}^{g,e}(\mathbf{R}_{HO}) \\ \widehat{H}_{diab}^{r,p}(\mathbf{R}_{HO}) &= \widehat{T}_{nuc}(\mathbf{R}_{HO}) + \widehat{V}_{diab}^{r,p}(\mathbf{R}_{HO})\end{aligned}\quad (5)$$

where \widehat{T}_{nuc} is the nuclear kinetic energy. The adiabatic system requires the addition of the nonadiabatic coupling to obtain the total Hamiltonian for the coupled electronic states:

$$\widehat{H}_{adia}^{tot} = \widehat{H}_{adia}^{g,e} + \widehat{\mathbf{d}}_{mn} \quad (6)$$

Specifically, $\widehat{\mathbf{d}}_{mn}$ is the derivative nonadiabatic coupling, given by the expression

$$\widehat{\mathbf{d}}_{mn} = -\sum_i \langle \psi_n^e(\mathbf{R}_i) | \widehat{\nabla} | \psi_m^g(\mathbf{R}_i) \rangle \cdot \Delta \mathbf{R}_i \quad (7)$$

where ψ_m^g and ψ_n^e are the adiabatic wavefunctions of the ground state and excited state, respectively. As is common practice,⁵ we omit the second derivative, or scalar, coupling for computational tractability, based on the knowledge that it is almost always smaller in magnitude than the derivative coupling.¹²³ However, there are many situations in which it cannot be neglected. The scalar coupling is undoubtedly important for the highest accuracy nonadiabatic dynamics, especially in detailed studies of specific molecules—but it is far less critical in general models with low

dimensionality, where omission causes negligible variations.¹²⁴ In contrast, the diabatic system does not require the nonadiabatic coupling, and instead depends on the linear coupling $\widehat{\mathbf{d}}_{diab}$.

We then simulated nonadiabatic dynamics with coherent vibrational wavepackets. All simulations were run with time steps of 0.2 fs or 0.4 fs for a duration of 2.0 ps or longer, which ensured that all significant dynamics had been completed. We use a Gaussian function to model a wavepacket excited to the higher electronic state at the Franck-Condon position. Time dependence is applied to the wavepacket using time coefficients (c_n) that include phase factors of $e^{-iE_n(t)}$. Here, \mathbf{n} is used to index all vibrational levels of both electronic states from $[0..m..n]$. The dynamics are described by the total time-dependent wavefunction,

$$|\Psi(\mathbf{R}, t)\rangle = \sum_{\mathbf{n}} c_{\mathbf{n}}(t) |\psi_{\mathbf{n}}(\mathbf{R})\rangle \quad (8)$$

The adiabatic system can be distinguished in terms of the wavefunctions on the adiabatic ground and excited states, while the diabatic system describes the wavefunctions on the diabatic reactant and product states:

$$\begin{aligned}|\Psi_{adia}(\mathbf{R}, t)\rangle &= \sum_m c_m^g(t) |\psi_m^g(\mathbf{R})\rangle + \sum_n c_n^e(t) |\psi_n^e(\mathbf{R})\rangle \\ |\Psi_{diab}(\mathbf{R}, t)\rangle &= \sum_k c_k^r(t) |\psi_k^r(\mathbf{R})\rangle + \sum_l c_l^p(t) |\psi_l^p(\mathbf{R})\rangle\end{aligned}\quad (9)$$

based on the states defined as shown in Fig. 3.

The geometric phase effect is a property unique to conical intersections in the adiabatic representation that is critical for accurate nonadiabatic dynamics, which attributes a phase of opposite sign to a wavefunction that travels a complete circular path around a conical intersection.^{3,125} In other words, two portions of an adiabatic wavepacket traveling on different sides of the conical intersection will attain opposite phases. We incorporated the geometric phase using a method detailed in refs. 125–127. The phase factor is calculated as $e^{i\theta}$, where θ is the rotation angle,

$$\theta = \arctan\left(\frac{2\widehat{\mathbf{d}}_{diab}}{\widehat{V}_{diab}^p - \widehat{V}_{diab}^r}\right) \quad (10)$$

The geometric phase factors were then applied to the adiabatic wavefunctions to obtain accurate nonadiabatic wavepackets.

As illustrated in Fig. 4, the coefficients for each state from eqn (9) can be used to determine the total wavepacket populations over time in the adiabatic excited and ground states, $c_{adia}^g(t)$ and $c_{adia}^e(t)$ (after geometric phase is applied), or in the diabatic reactant and product states, $c_{diab}^r(t)$ and $c_{diab}^p(t)$:

$$\begin{aligned}c_{adia}^{g,e}(t_0..t_f) &= \sum_{m,n} c_{m,n}^{g,e}(t_0..t_f) \\ c_{diab}^{r,p}(t_0..t_f) &= \sum_{k,l} c_{k,l}^{r,p}(t_0..t_f).\end{aligned}\quad (11)$$

Parallel calculations are used for both the adiabatic and diabatic systems, but the diabatic system does not include the nonadiabatic coupling as shown in eqns (6)–(7), or the geometric phase in (10), which only apply in the adiabatic representation.

Table 1 Properties of conical intersection topography models. Minimum and maximum values achieved in each Δv series for total nonadiabatic transfer to the ground state (Ψ_{total}^g), time required for nonadiabatic transfer (t_{total}), and ground-state product formation ($\Psi_{product}^g$), where Ψ_{total}^g and $\Psi_{product}^g$ are percentages of the total wavepacket; and energies at key locations – the conical intersection point (E_{CI}), the excited-state minimum (E_{min}^e), the excited-state Franck-Condon position (E_{FC}), and the ground-state product minimum (E_{min}^p). Arrows indicate the direction of change with respect to Δv from $v_{min} \rightarrow v_{max}$.

model	series	Δv	ground-state total Ψ_{total}^g (min, max)	transfer time t_{total} (min, max)	E_{CI} (eV)	E_{min}^e (eV)	E_{FC} (eV)	ground-state product $\Psi_{product}^g$ (min, max)	E_{min}^p (eV)
1P	Δv_{xy}	9→18 THz	88→80 %	88 → 23 fs	0.22	0.22	0.88→0.83		
	Δv_{xy}	6→20 THz	80→72 %	604→58 fs					
	Δv_x	4→20 THz	79→72 %	788→57 fs	2.05	1.70	2.42		
1S	Δv_y	4→20 THz	80→72 %	820→92 fs					
	Δv_{xy}	6→20 THz	84→77 %	142→27 fs				30→44 %	
	Δv_x	4→20 THz	82→80 %	195→36 fs	0.50	0.50	1.61	13→42 %	0.32
2P	Δv_y	4→20 THz	85→77 %	177→72 fs				37→47 %	
	Δv_{xy}	8→15 THz	69→78 %	104→68 fs	1.10	1.06→0.74	3.32→1.77	17→39 %	
	Δv_x	6→20 THz	74→79 %	141→47 fs	1.10	0.88	2.38	18→42 %	0.40
2S	Δv_y	6→20 THz	80→74 %	212→66 fs	0.75→1.89	0.38→0.84	2.02	30→34 %	

We assessed three primary variables from nonadiabatic dynamics: the total nonadiabatic wavepacket transfer to the ground state, the time at which nonadiabatic transfer is completed, and (in product-forming models) the yield of ground-state photoproduct resulting from nonadiabatic transfer (Table 1). We quantify the time of nonadiabatic transfer completion by identifying the point at which the ground- and excited-state wavepacket populations first begin to stabilize near their average final values. We determine the nonadiabatic transfer and product yields as the percentages of the *total* wavepacket population—occupying the ground state, and occupying the ground state with the chemical character of the product, respectively. In the next section, we discuss the results from these calculations with respect to quantitative changes in topography. Note that the potential energy surfaces and wavepacket dynamics will be shown in the *adiabatic* representation in the results to follow, for consistency as well as a more accurate depiction of the conical intersection. The data listed in Table 1 summarizes the key properties and results from the four conical intersection models, and can be referenced throughout the discussion.

4 Results and discussion

4.1 Peaked with one path, 1P

In the peaked topography with one path, nonadiabatic transfer from the excited state leads to the ground state, which is topographically simple and has one energetic minimum corresponding to one molecular species, the reactant (Fig. 5a). The standard double cone shape formed by the intersection is shown in Fig. 5b for the 1P model, in which the tip of the funnel corresponds to the conical intersection point at the minimum on the excited state potential energy surface. As shown, we constructed the model with moderate to high symmetry and only a slight degree of tilt to preserve the peaked topography.

We found that applying frequency changes to just one coordinate as v_x or v_y alone did not maintain the single ground-state minimum and caused it to bifurcate, so that the intended single molecular pathway was branched into two pathways. For this reason, we discuss only equivalent and symmetric changes

to both frequency parameters simultaneously (Δv_{xy}) for this category, with a range from 9–18 THz. The effect is that higher frequencies induce greater curvature in the potential energy surface topography (Fig. 5a), with a similar effect on the conical intersection topography, inducing a sharper slope in the funnel descending toward the intersection on the excited state, and away from the intersection on the ground state (Fig. 5b). These changes in frequency from 9–18 THz correspond to minimal changes in the total tilt angle (α) from 2.5–5.3°, and changes in the cylindrical symmetry (Δ_{gh}) from 0.1–0.5 (where $\Delta_{gh} = 0$ indicates perfect symmetry).^{53,54}

4.1.1 Extent of nonadiabatic transfer in 1P.

Dynamics simulations incorporating these incremental changes in topography show that reducing the slope by decreasing v_{xy} causes the total extent of nonadiabatic transfer to steadily increase (Fig. 5c). A substantial portion of the wavepacket population decays to the ground state, increasing from 80–88% as v_{xy} decreased from 18 THz to 9 THz. This appears somewhat counter-intuitive, because it seems that a greater slope, which makes pathways descending toward a peaked conical intersection more dynamically favorable, would actually facilitate nonadiabatic transfer by accumulating more wavepacket momentum and directing it toward the intersection more effectively. However, the results are clearly explained by the fundamental importance of the potential energy difference: more gradual slopes increase the area where the potential energy surfaces are close in energy. We observe that with a greater slope induced by higher frequency values, the energy gap increases more sharply with the distance from the conical intersection, therefore reducing the area where nonadiabatic coupling is effective and decreasing the extent of transfer overall.

This result may appear to contrast with results from previous work, which demonstrated that descent in a direction with steeper variation in energy gap between the two surfaces and greater descent velocity results in higher probabilities of nonadiabatic transition.²⁸ The prior study focused on varying the *direction* of approach to the conical intersection in a set topography, whereas here we vary the topography itself to contribute and ex-

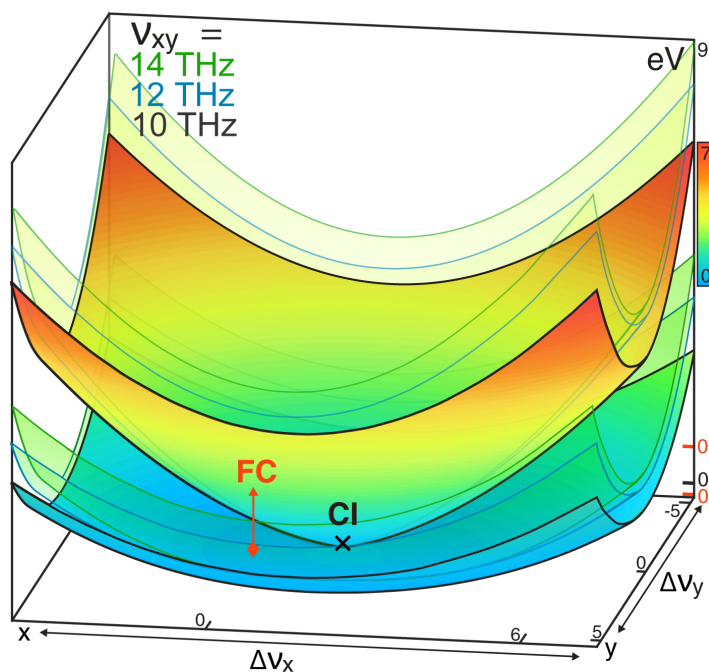
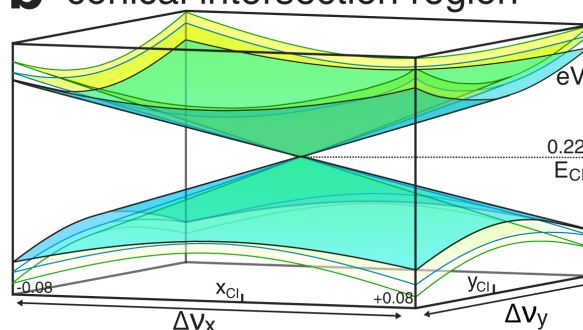
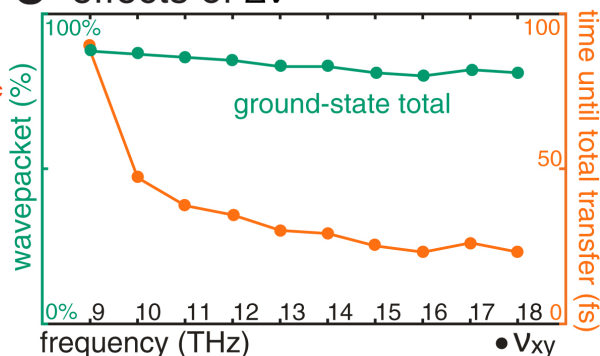
a potential energy surfaces**b** conical intersection region**c** effects of Δv 

Fig. 5 Peaked topography with one path, 1P. (a) Example potential energy surfaces from the 1P model, showing the adiabatic electronic ground state and excited state. The surfaces shown in gradient color with black edges were calculated with $v_{xy} = 10$ THz. The ground-state reactant minimum (\blacklozenge) also corresponds to the region of Franck-Condon excitation (\uparrow FC) to 0.87 eV on the excited state. The conical intersection (\times CI) is located at the minimum of the excited state at 0.22 eV. Overlaid transparent surfaces with blue and green edges show examples of modified topographies with $v_{xy} = 12$ THz and 14 THz. (b) Larger view of conical intersection topography, from the same potential energy surfaces shown in (a) with $v_{xy} = 10$ THz, 12 THz, and 14 THz. (c) Trends in nonadiabatic transfer properties of 1P topographies with simultaneous changes to both frequencies, v_{xy} (\bullet), from 9–18 THz. Plot shows the total percentage of the wavepacket population that undergoes nonadiabatic transfer to the ground state (green), and the time until the amount of nonadiabatic transfer begins to stabilize (orange) from dynamics simulations.

pand upon previous findings. They found that faster wavepacket velocities decrease the width of the wavepacket trajectory distribution, causing a reduction in the average potential energy gap encountered and therefore a higher transition probability—thus our conclusions and those of the prior study nonetheless cite the same fundamental principle. The differing observations are likely derived from the difference in methodology: here we examine the entire decay process for a single wavepacket, including multiple passages through the conical intersection if they occur, instead of examining the first passage in many trajectories. Also of note is that the former study used the Landau–Zener equation for calculation of the transition probability—which is widely used, but limits the context to linear trajectories over a one-dimensional crossing.¹²⁸ Therefore the Landau–Zener treatment only allows transitions at a single crossing point and does not account for the broader influence of nonadiabatic coupling spread throughout the conical intersection region, nor the gradual nonadiabatic transfer and electronic-state mixing this can induce.^{7,129}

4.1.2 Rate of nonadiabatic transfer in 1P.

All of our simulations also show that 1P topographies achieve nonadiabatic transfer with extremely fast rates, as indicated by the amount of time required for nonadiabatic transfer to stabilize (Fig. 5c). In these models, nonadiabatic transfer approached

completion within times on the scale of ~ 20 – 100 fs, with the fastest rate (23 fs) achieved by the topography in which the frequencies were maximized at 18 THz—which also yielded one of the lowest amounts of transfer (81%). These timescales approach some of the fastest rates observed in conical intersections—with the ideal topography found in Jahn-Teller intersections, nonadiabatic transfer is completed on the scale of 10–20 fs or less.^{130,131}

Overall, greater values of v_{xy} induced faster rates of nonadiabatic decay, because steeper slopes attribute more momentum to the wavepacket and promote more rapid descent from the excitation region to the energetic minimum of the peaked conical intersection. Greater extents of nonadiabatic transfer were achieved, however, by lower v_{xy} values and slower wavepacket dynamics approaching the conical intersection. This can be attributed not only to the static effect on the region of effective nonadiabatic coupling already discussed, but also to dynamic effects. We observed that less rapid wavepacket dynamics maintained wavepacket formation and collected the wavepacket around the intersection region more effectively, whereas more rapid dynamics tended to scatter and fragment the wavepacket as it first reaches the conical intersection. This dynamic behavior further explains the increased nonadiabatic transfer that we observed with lower slopes leading to the peaked conical intersection.

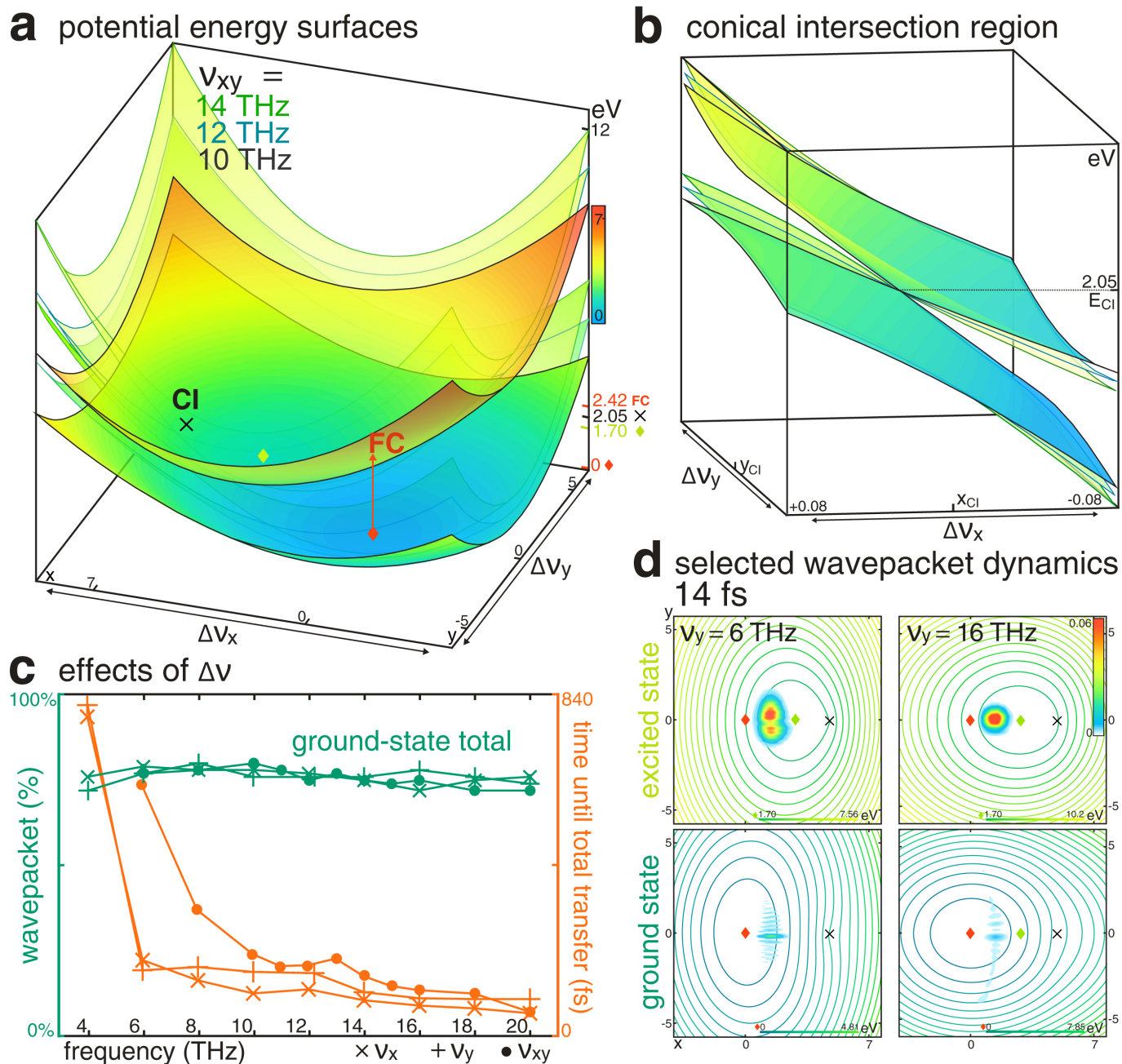


Fig. 6 Sloped topography with one path, 1S. (a) Example potential energy surfaces from the 1S model, showing the adiabatic electronic ground state and excited state. The surfaces shown in gradient color with black edges were calculated with $v_{xy} = 10$ THz. The ground-state reactant minimum (◆) corresponds to the region of Franck-Condon excitation (↑ FC) to 2.42 eV on the excited state. The conical intersection is located at 2.05 eV (× CI), and does not coincide with the excited-state minimum at 1.70 eV (◆). Overlaid transparent surfaces with blue and green edges show examples of modified topographies with $v_{xy} = 12$ THz and 14 THz. (b) Larger view of conical intersection topography, from the same potential energy surfaces in (a) with $v_{xy} = 10$ THz, 12 THz, and 14 THz. (c) Trends in nonadiabatic transfer properties of 1S topographies with changes in v_x (×), v_y (+), and v_{xy} (●), within 4–20 THz. Plot shows the total percentage of the wavepacket population that undergoes nonadiabatic transfer to the ground state (green) and the time until the amount of nonadiabatic transfer begins to stabilize (orange) from dynamics simulations. (d) Example wavepacket dynamics at 14 fs from simulations in two 1S topographies: $v_x = 12$ THz, $v_y = 6$ THz (left panels) and $v_x = 12$ THz, $v_y = 16$ THz (right panels). Contour plots show the wavepacket density (color gradient) on the excited state (top) and ground state (bottom) potential energy surfaces, where the conical intersection (×), excited-state minimum (◆), and ground-state minimum/excited-state Franck-Condon position (◆) are labeled.

4.2 Sloped with one path, 1S

Next we examine sloped conical intersections in their standard role. Sloped topographies are known for conferring photostability through nonadiabatic transfer leading to a single path on the ground state that regenerates the reactant. This model performs

the same function as the peaked model 1P, discussed above, although the conical intersection and potential energy surface topographies are distinct. As in peaked topographies, increasing v_x and v_y induces more curvature in the potential energy surfaces containing a sloped conical intersection (Fig. 6a). However, an

important difference in their effects, shown in Fig. 6b, is that greater frequencies increase the unfavorable uphill slope leading to a sloped intersection, in contrast to increasing the favorable downhill slope leading to a peaked intersection. In the sloped model, v_x also has a greater impact on the slope than v_y , because the x -coordinate corresponds to the reaction coordinate from the region of Franck-Condon excitation to the conical intersection. This is evidenced by their effects on the tilt of the conical intersection. In this model, changes in v_x from 4–20 THz caused the total tilt angle to increase from 27–50°, while changes in v_y from 4–20 THz modified the tilt to a lesser extent from 37–50°.

Nonetheless, dynamics simulations in the sloped model show similar general trends in the timescale and extent of nonadiabatic transfer as in peaked model with one path. Overall, the total extent of transfer increases as frequency decreases, but this is also accompanied by an increase in the time required for transfer (Fig. 6c). As expected for conical intersections that are less energetically favorable than the **1P** topography, reduced nonadiabatic transfer from 72–80% was accomplished on much longer timescales—within a larger range from ~60–800 fs. These results are consistent with the concept that the local topography around the conical intersection has a greater influence on dynamics in conditions where kinetic energy is low,²⁸ which is common in the presence of less energetically favorable conical intersections.³⁰

4.2.1 Extent of nonadiabatic transfer in **1S**.

For this topography class, we examine changes in v_x or v_y individually in addition to concurrent changes in both parameters (v_{xy}). We found that increases in all three series, v_x , v_y , and v_{xy} , reduced the efficacy of the conical intersection and decreased the total amount of nonadiabatic transfer (Fig. 6c). For example, $\Delta v_{xy} = 10$ –20 THz caused total transfer to decrease from 80–72%. This trend can also be explained by the reduced area of non-negligible nonadiabatic coupling, which results as the branching frequencies are increased and the potential energy gap surrounding the intersection becomes greater. The trend is more consistent and slightly more substantial with v_y , compared to v_x , and furthermore is most substantial with v_{xy} —indicating that v_x and v_y exert distinct and additive topographical effects.

We find that lower frequency parameters that minimize the energy gap are more effective for nonadiabatic transfer regardless of the type of topography—up to a limit. Starting at 6 THz for v_x and 8 THz for v_y , the extent of nonadiabatic transfer begins to decrease with lower frequencies (Fig. 6c). This is an important effect relevant to less energetically favorable conical intersections such as sloped topographies. Unlike in peaked intersections, our dynamics simulations of the **1S** model show that if the frequency is too low or the excited-state surface is not steep enough (v_x , $v_y = 4$ THz, for example), the wavepacket does not accumulate enough momentum while descending from the Franck-Condon region to access the conical intersection as effectively. This is also the case if the conical intersection is very distant from the excitation region or very high in energy, meaning more momentum is required for the wavepacket to propagate to the intersection location.³⁰ Overall, these results show that the branching frequencies affect the capacity for nonadiabatic transfer in a parallel manner

for both peaked and sloped intersections—unless the frequencies are low enough, in sloped intersections, that the less favorable location of the conical intersection becomes a factor.

The data here corroborates previous conclusions that sloped conical intersections are not inherently less effective for nonadiabatic transfer than peaked intersections,²⁸ as indicated by the substantial nonadiabatic transfer achieved in the sloped models, comparable to typical results from peaked topographies. These observations further emphasize that it is not the topography itself, but the *dynamic effects* it induces, that are responsible for any differences in nonadiabatic transfer efficacy observed in peaked versus sloped intersections.²⁸ We elaborate on the dynamic effects next in discussing the nonadiabatic transfer rate.

4.2.2 Rate of nonadiabatic transfer in **1S**.

The changes observed in the amount of nonadiabatic transfer also correspond to more dramatic changes in the time required for transfer in **1S** topographies. Results were consistent with increasing v_x , v_y , and v_{xy} (Fig. 6c), all of which reduced the time required for wavepacket transfer due to the increase in the slope of the potential energy surfaces. Like in peaked topographies, greater slopes allow the wavepacket to accumulate more momentum and propagate more rapidly toward the conical intersection. We observed that the transfer rate is slightly more dependent on v_x , which achieved faster timescales ranging from 788 fs to 57 fs, than v_y , which reduced the timescale from 820 fs to 92 fs. The influence of v_x is prominent because it alters topography along the axis of the reaction coordinate, which includes the pathway of descent from the Franck-Condon region to the excited-state minimum followed by ascent to the conical intersection, and determines the momentum of the wavepacket as it traverses this coordinate. The impact of v_y on the transfer rate is less straightforward, because it does not affect the reaction coordinate topography. Increasing v_y induces greater curvature and a steeper upward slope along y in both directions away from the minimum, which is aligned with the conical intersection in y (Fig. 6a). This forms a narrower valley of low potential that is favorable for wavepacket dynamics in y , as demonstrated in Fig. 6d, therefore restricting wavepacket motion and delocalization along the y -coordinate and instead favoring use of wavepacket momentum along the x -coordinate—toward the conical intersection.

The much wider range of timescales for nonadiabatic transfer observed here demonstrates that slight changes in topography around a sloped conical intersection can significantly impact the resultant dynamics and transfer rate of a photochemical process. These results also support the conclusion that less energetically favorable conical intersections like sloped topographies are more sensitive to wavepacket momentum—and the topographical parameters that determine it. Notably, we also observe that the most substantial increases in transfer time coincide with the low frequency values (≤ 6 THz, 8 THz) that did not follow the primary trend in total nonadiabatic transfer, causing it to decrease. For example, the time required for nonadiabatic transfer to plateau was lengthened dramatically to 788 fs with $v_x = 4$ THz and roughly 820 fs with $v_y = 4$ THz (Fig. 6c), after which gradual transfer actually continued until about 1.5 ps in both cases. With v_{xy}

= 6 THz, initial nonadiabatic transfer was achieved in 604 fs, but transfer was not fully completed for roughly 1.75 ps. This is consistent with our conclusions that lower branching frequencies reduce the accumulation of wavepacket momentum, and that without enough momentum, wavepacket exposure to nonadiabatic coupling is impeded—thus corresponding to reduced nonadiabatic transfer requiring significantly longer timescales.

4.3 Peaked with two paths, 2P

Next we examine the prominent role of peaked topographies in mediating photoreactions. This case is topographically similar to the peaked model with one path (1P), but with the addition of a second minimum on the ground state that corresponds to the photoproduct species and is separated from the reactant minimum by a potential energy barrier (Fig. 7a). The product region is more distant along the reaction coordinate (x) than the conical intersection and is accessible following nonadiabatic transfer to the ground state. We constructed these models with a product that is 0.32 eV higher in energy than the reactant, and simulate a common reaction pathway in which conversion to a higher-energy chemical species is made possible through a conical intersection. For simplicity, we model only the forward reaction in which the lower-energy species is excited, and not the reverse reaction. Manipulation of the vibrational frequencies affects the topography in the same manner as in the 1P model, with an additional effect. As seen in Fig. 7b, the tilt of the conical intersection is more noticeable, in contrast to the minimal tilt in the one-path topography. In the two-path model, the two ground-state minima cause an inherent tilt in the conical intersection along the x -coordinate as the potential energy increases from reactant to product. Therefore, the frequency parameters, especially ν_x , modulate the tilt angle more extensively. Varying ν_x from 4–20 THz caused the tilt angle to increase from 5.4–11.4°, while varying ν_y from 4–20 THz caused increases from 10.3–12.6°. Furthermore, the same changes in ν_x had a substantial impact on the intersection symmetry, which varied from $\Delta_{gh} = 0.15$ (toward symmetry) to 0.94 (high asymmetry).

4.3.1 Extent of nonadiabatic transfer in 2P.

The dynamics simulations in 2P topographies reveal trends that are consistent with the previous two cases: Decreasing the branching frequencies increases the total extent of nonadiabatic transfer achieved, but also requires longer relaxation times (Fig. 7c). Here, we observed amounts of nonadiabatic transfer ranging from 77–85%. Increases in the total extent of transfer are evident with decreases in ν_x , ν_y , or ν_{xy} , although the amount was much less sensitive to $\Delta\nu_x$ in this model, ranging from 80–82% with frequencies from 20 THz to 4 THz. We can again attribute the reduced extent of transfer occurring with higher frequencies to the reduction in regions where the two potential energy surfaces are close in energy and exhibit non-negligible nonadiabatic coupling.

In addition to static changes in potential energy surface topography, dynamic effects also contribute to the reduction in nonadiabatic transfer induced by greater frequencies. Higher frequencies reduce wavepacket exposure to nonadiabatic coupling during dynamics, for several reasons. Wavepackets that traverse the

potential energy surfaces more rapidly (due to greater slopes) necessarily spend less time moving through regions of nonadiabatic coupling. Furthermore, wavepackets with greater momentum are more capable of dynamics through less energetically favorable regions—in peaked topographies, these are regions farther from the favorable conical intersection. Therefore high-energy dynamics can reduce exposure to the nonadiabatic coupling around the intersection (in contrast to the effect in sloped intersections, where additional momentum is often beneficial in accessing the conical intersection). For example, we observe that high-momentum wavepackets sometimes move past a peaked conical intersection on the x -coordinate after reaching its location, so multiple passages over the intersection can be necessary to accumulate comparable nonadiabatic transfer. In addition, the simulations show that a steeper slope increases the wavepacket's tendency to scatter and fragment on the excited state upon reaching the conical intersection, as shown in Fig. 7d with $\nu_{xy} = 16$ THz. This dynamic behavior was also evident with higher frequencies in the peaked model with one path (1P), but it was less noticeable due to the very short distance to the conical intersection. We observe scattering and partial deflection of the wavepacket in peaked topographies because the slope inverts at the intersection on the excited state, and acts as a potential energy barrier if the slope is steep enough. Scattered fragments of the wavepacket are delayed in reaching the conical intersection and must retrace part of their trajectory, which contributes to a less efficient and less complete initial nonadiabatic transfer process. This contrasts with the smooth descent of a more substantial population to the ground state, promoted by gradual slopes that minimize wavepacket delocalization, as shown in Fig. 7d with $\nu_{xy} = 10$ THz.

4.3.2 Rate of nonadiabatic transfer in 2P.

As for the previous examples, we found that lower frequencies of ν_x , ν_y , or ν_{xy} that achieve greater nonadiabatic transfer also correspond to longer transfer times, ranging from ~30–200 fs (Fig. 7c). These rates are consistent with those measured experimentally for molecules in this class, like rhodopsin, for which an excited-state lifetime of 50 fs¹³² and appearance of photoproduct within ~30 fs have been observed.^{106,133} In more detail, our simulations indicate that the duration of nonadiabatic transfer is most dependent on ν_x , which decreased transfer rates from 195 fs (at 4 THz) to 36 fs (at 20 THz). Again, higher ν_x values promote accumulation of momentum and more rapid wavepacket dynamics along the reaction coordinate toward the conical intersection, and subsequently the ground-state product region. Meanwhile, higher ν_y values limit wavepacket dynamics in the y -dimension and facilitate a more direct trajectory along the x -coordinate. As in the 1S topography, however, ν_y was less effective at promoting faster transfer rates, which varied from 177 fs (at 4 THz) to 72 fs (at 20 THz). Furthermore, the transfer rate was modulated most substantially by ν_{xy} , compared to equivalent frequency ranges for ν_x or ν_y alone. This result further emphasizes that the two coordinate frequencies exert distinct topographical and dynamic effects, which are compounded when both frequencies are changed simultaneously.

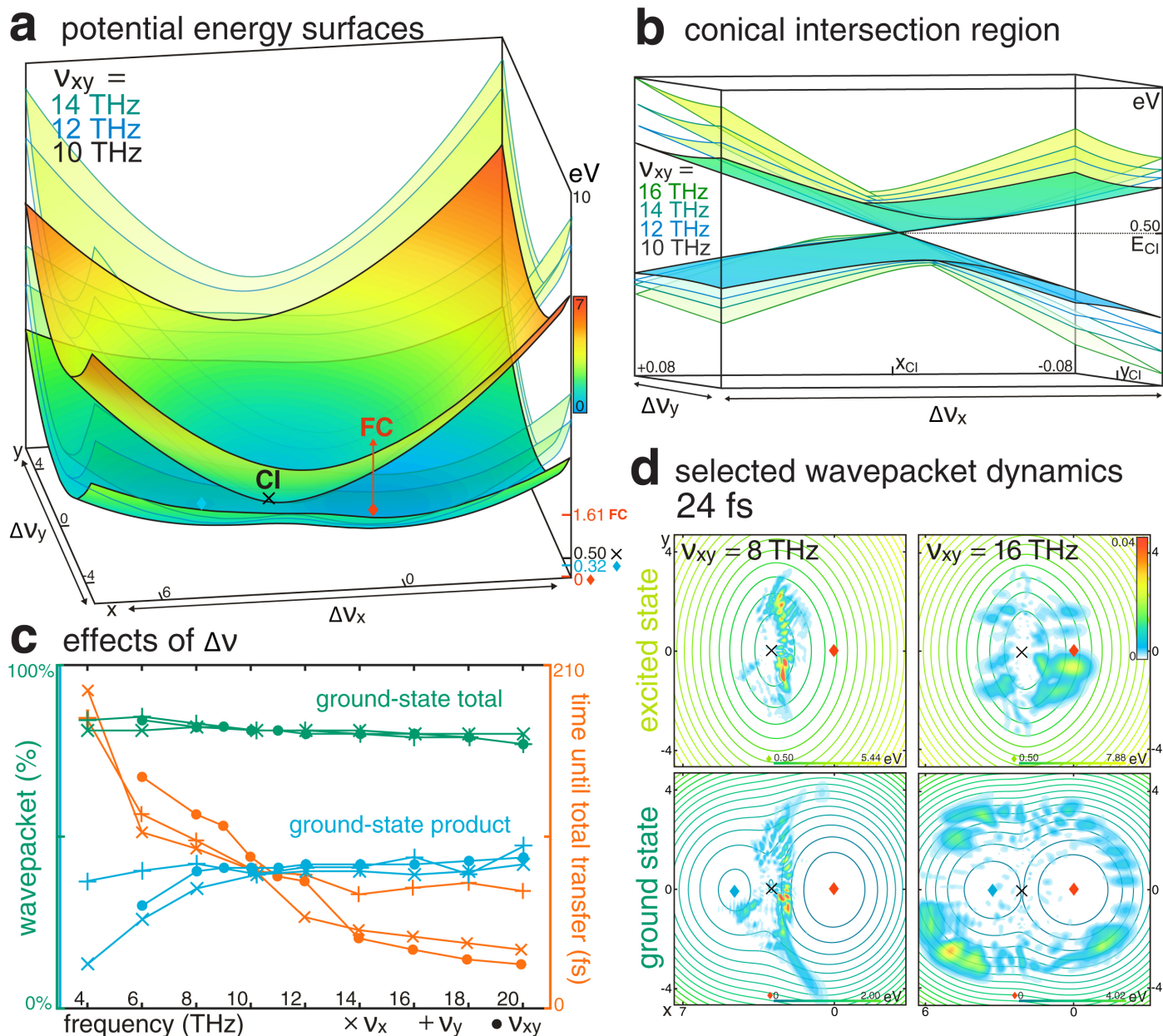


Fig. 7 Peaked topography with two paths, 2P. (a) Example potential energy surfaces from the 2P model, showing the adiabatic electronic ground state and excited state. The surfaces shown in gradient color with black edges were calculated with $v_{xy} = 10$ THz. The ground-state reactant minimum (\blacklozenge) corresponds to the region of Franck-Condon excitation (\uparrow FC) to 1.61 eV on the excited state. The second path leads to formation of the product, corresponding to a local ground-state minimum of 0.32 eV (\blacklozenge). The conical intersection (\times CI) is located at the excited-state minimum at 0.50 eV. Overlaid transparent surfaces with blue and green edges show examples of modified topographies with $v_{xy} = 12$ THz and 14 THz. (b) Larger view of conical intersection topography, from the same series of potential energy surfaces in (a), with $v_{xy} = 10$ THz, 12 THz, 14 THz, and 16 THz. (c) Trends in nonadiabatic transfer properties of 2P topographies with Δv_x (\times), Δv_y ($+$), and Δv_{xy} (\bullet), within 4–20 THz. Three variables from dynamics simulations are plotted: the total percentage of the wavepacket population that undergoes nonadiabatic transfer to the ground state (green), the percentage of the wavepacket population that forms photoproduct after nonadiabatic transfer (blue), and the time until the amount of nonadiabatic transfer begins to stabilize (orange). (d) Example wavepacket dynamics at 24 fs from simulations in two 2P topographies: $v_{xy} = 8$ THz (left panels) and $v_{xy} = 16$ THz (right panels). Contour plots show the wavepacket density (color gradient) on the excited state (top) and ground state (bottom) potential energy surfaces, where the conical intersection (\times), ground-state reactant minimum/excited-state Franck-Condon position (\blacklozenge), and ground-state product minimum (\blacklozenge) are labeled.

4.3.3 Photoproduct formation in 2P.

For topographies that allow product formation after transfer to the ground state, we also measure the photoproduct yield (as the percent of the total wavepacket population that ultimately sta-

bilizes with ground-state product character). In contrast to the amount of nonadiabatic transfer, we observe that the photoproduct yield increases with an increase in v_x , v_y , or v_{xy} and shows a stronger dependence on frequency, ranging from 13–47% overall (Fig. 7c). Despite the concurrent decrease in the extent of

nonadiabatic transfer, increasing ν_x or ν_y has a more prominent effect on the distribution of the ground-state wavepacket after transfer that promotes a net increase in photochemical quantum yield—thus illustrating the remarkable functionality of conical intersection topography in modulating photoreactions. Increasing the frequency in the x -dimension induces a steeper slope along the reaction coordinate toward the intersection, and toward the photoproduct region located farther along the x -coordinate on the ground state. Therefore greater ν_x values direct the wavepacket to the product more effectively, resulting in greater photoproduct yields from nonadiabatic transfer. For these reasons, the product yield is most dependent on ν_x and increased from 13–42% as the frequency increased from 4–20 THz. Along the other coordinate, an increase in ν_y again reduces wavepacket motion within the y -direction and assists in directing the wavepacket along x . As a result, product formation is less dependent on ν_y and varied from 37–47% (4–20 THz), clearly indicating that the two frequencies influence the product yield individually.

4.4 Sloped with two paths, 2S

The sloped topography with two paths is more complicated, and illustrates the complex interplay between topographical properties and dynamic effects that ultimately determines reaction outcomes. To construct this topography, the intersection location must be displaced from the reactant-to-product path in order to achieve the necessary slope at the conical intersection. Therefore we have constructed the **2S** potential energy surfaces (Fig. 8a) with the product region displaced from the reactant in the x -coordinate, as in the previous models, but in addition the conical intersection is displaced in the y -coordinate (although still at the origin in x). As a result, compared to the **1S** sloped model, it is primarily ν_y , instead of ν_x , that influences the tilt angle and the uphill slope leading to the conical intersection (Fig. 8b). Quantitatively, increases in ν_y from 6–20 THz induced substantial changes in the tilt angle from 20–57°. An increase in ν_x exaggerates the slope along the product-forming coordinate, but has much less effect on the conical intersection topography because it is insubstantially tilted in x . As a result, ν_x had minimal impact on the total tilt angle, which varied negligibly (few degrees), although ν_x did modify the symmetry from $\Delta_{gh} = 0.60$ –0.95 as it varied from 6–20 THz.

4.4.1 Extent of nonadiabatic transfer in 2S.

As shown in Fig. 8c, simulations with the **2S** model obtained total nonadiabatic transfer yields from 69–80% within moderate timescales from ~50–200 fs. In contrast to the other three models, however, this topography shows an opposite trend in which nonadiabatic transfer *increases* with increasing ν_x (from 74–79% with 6–20 THz) and ν_{xy} (from 69–78% with 8–15 THz). Yet with increasing ν_y , the extent of nonadiabatic transfer decreases, consistent with the previous models. Similarly, this can be attributed to the greater area of significant nonadiabatic coupling due to a reduced energy gap. In addition, because the conical intersection is displaced and sloped in the y -direction, lower ν_y frequencies remain beneficial for nonadiabatic transfer because they reduce the uphill energetic gradient and the tilt of the conical intersection

in y —whereas the slope in x does not pose a significant energetic obstacle.

As for the x -coordinate, reduced slopes actually impede nonadiabatic transfer in this model. One reason is that $\Delta\nu_x$ affects the initial energy of the wavepacket because it alters the surface topography in the x -dimension (in which the excited-state surface is displaced)—and therefore the energy of the Franck-Condon position to which the wavepacket is initially excited. The Franck-Condon location remains consistent in y , so ν_y does not affect the initial wavepacket energy. Therefore we can conclude that the reduced initial wavepacket energy caused by lower ν_x values contributes to the reduced extent of nonadiabatic transfer in this topography, where the sloped conical intersection is less favorable for wavepacket access.

Based on this reasoning we might expect similar behavior in the **1S** model, but we did not observe the same reverse trend in nonadiabatic transfer. Two factors explain this result. First, the excited state must be much less displaced in the previous model to maintain the single reaction path, so the initial wavepacket energy is less dependent on ν_x in **1S**. The second contribution to the distinct effects of ν_x again results from the importance of the potential energy gap. Examination of the energy difference in the coordinate space (Fig. 8d) shows that greater ν_x values effectively elongate the region where the potential energy surfaces are close in energy, expanding the area of effective nonadiabatic coupling along the y -axis—in contrast to the previous three models, in which the potential energy difference is minimized with *lower* frequencies of ν_x or ν_y . Furthermore, based on the wavepacket trajectories plotted in Fig. 8d, greater ν_x values appear to restrict the spread of excited-state wavepacket dynamics along the x -coordinate, confining them within the nonadiabatic coupling region that is narrow in x and elongated in y . These effects are evidenced quantitatively: increasing ν_x resulted in an increase in the overall nonadiabatic coupling in the area containing the excited-state wavepacket trajectory, from an average of 3.22 eV to 10.33 eV per coordinate unit with $\nu_x = 10$ THz and $\nu_x = 18$ THz, respectively. This also corresponds to an increase in the average nonadiabatic coupling experienced along the wavepacket trajectory, from 0.19 to 0.35 eV per femtosecond in the same two examples. In addition, the effects of ν_x were reproduced by ν_{xy} , which induced a parallel trend in the extent of nonadiabatic coupling. This provides further evidence of the important role of ν_x in this case—in contrast to the other models in which ν_y had a dominant influence on the total nonadiabatic transfer.

4.4.2 Rate of nonadiabatic transfer in 2S.

We observe that the duration of nonadiabatic transfer is consistent with trends in the other models, with longer times required as ν_x , ν_y , or ν_{xy} are reduced (Fig. 8c). The time required for transfer to complete ranged from its maximum of 212 fs to 66 fs with (increasing) $\nu_y = 6$ –20 THz, and from 141 fs to 47 fs with $\nu_x = 6$ –20 THz. In addition, the timescales increase significantly at low values of ν_y or ν_x around 6 THz, replicating results from the **1S** model due to the reduced energetic accessibility of sloped conical intersections. Furthermore, the individual dynamic effects of $\Delta\nu_x$ and $\Delta\nu_y$ on the transfer rate do not seem to be additive in

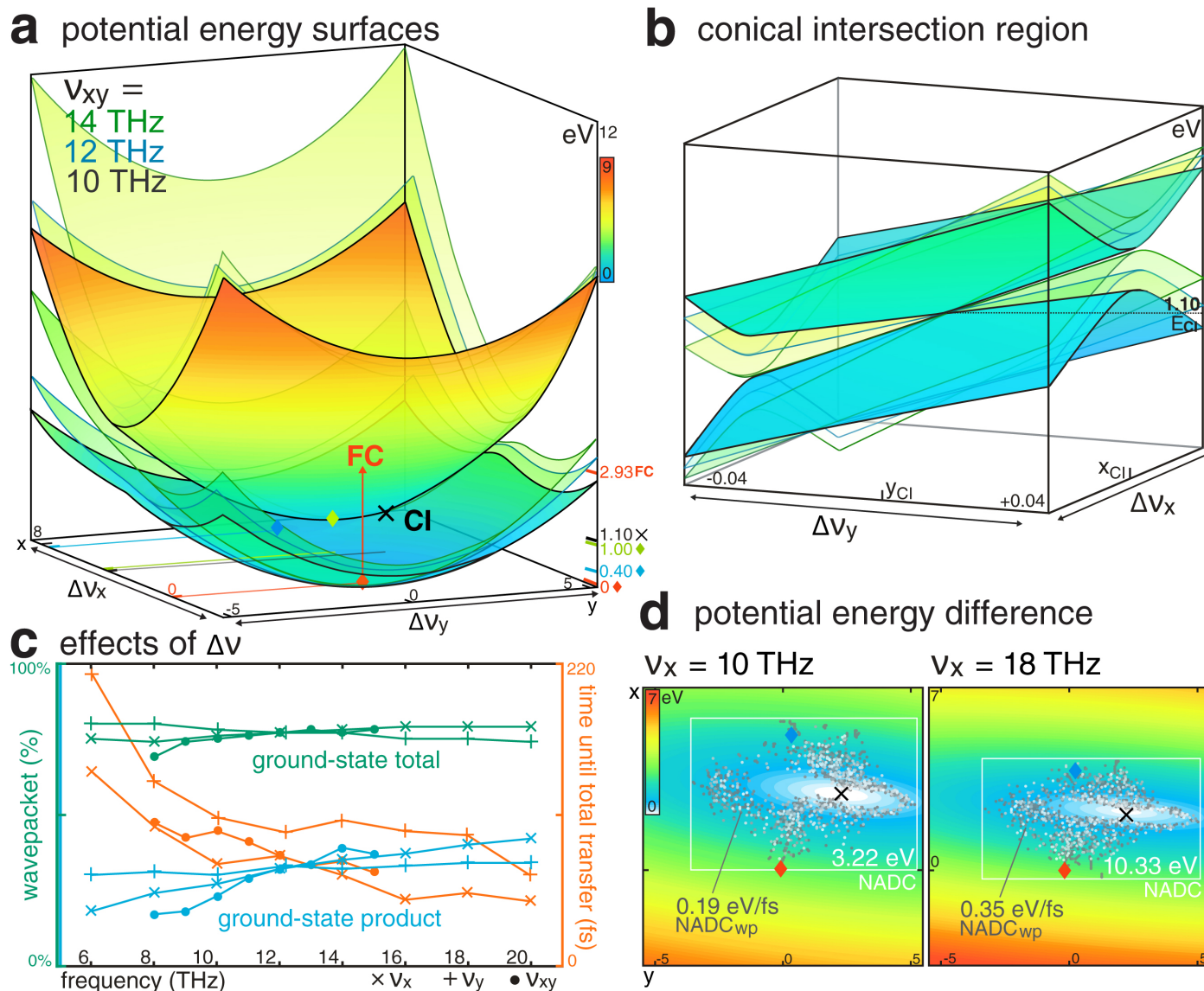


Fig. 8 Sloped topography with two paths, 2S. (a) Example potential energy surfaces from the 2S model, showing the adiabatic electronic ground state and excited state. The surfaces shown in gradient color with black edges were calculated with $v_{xy} = 10$ THz. The ground-state reactant minimum (\blacklozenge) corresponds to the region of Franck-Condon excitation (\uparrow FC) to 2.93 eV on the excited state. The second path leads to formation of the product, corresponding to a local ground-state minimum of 0.40 eV (\blacklozenge). The conical intersection (\times CI) is located at 1.10 eV, and is displaced from the excited-state minimum at 1.00 eV (\blacklozenge). Overlaid transparent surfaces with blue and green edges show examples of modified topographies with $v_{xy} = 12$ THz and 14 THz. (b) Larger view of conical intersection topography, from the same potential energy surfaces in (a) with $v_{xy} = 10$ THz, 12 THz, and 14 THz. (c) Trends in nonadiabatic transfer properties of 2S topographies with Δv_x (\times), Δv_y ($+$), and Δv_{xy} (\bullet), within 6–20 THz. Three variables from dynamics simulations are plotted: the total percentage of the wavepacket population that undergoes nonadiabatic transfer to the ground state (green), the percentage of the wavepacket population that forms photoproduct after transfer (blue), and the time until the amount of nonadiabatic transfer begins to stabilize (orange). (d) Contour plots of the energy difference between the adiabatic ground and excited state potential energy surfaces in two 2S topographies: $v_x = 10$ THz, $v_y = 12$ THz (left) and $v_x = 18$ THz, $v_y = 12$ THz (right). Markers (\bullet) indicate the location of the highest excited-state wavepacket density at 0.2 fs time points from 0–1 ps during simulations, with darker gray color indicating earlier times and lighter gray color indicating later times. Locations of the conical intersection (\times), ground-state reactant minimum/excited-state Franck-Condon position (\blacklozenge), and ground-state photoproduct minimum (\blacklozenge) are labeled. The average nonadiabatic coupling along the wavepacket trajectory from 0–1 ps (NADC_{wp}) was calculated to be 0.19 eV/fs for $v_x = 10$ THz (left), and 0.35 eV/fs for $v_x = 18$ THz (right). The area containing the wavepacket trajectory (white box) was calculated to have an average nonadiabatic coupling (NADC) of 3.22 eV (left) and 10.33 eV (right) per coordinate unit.

this case. When frequency changes are applied simultaneously as v_{xy} , we observe that the time required for transfer does not vary more substantially—likely due to the division of coordinates into the coordinate of the reaction pathway (x) and the coordinate of conical intersection displacement (y).

4.4.3 Photoproduct formation in 2S.

Lastly we examine the photoproduct yield, which consisted of 17–42% of the total wavepacket from initial excitation (Fig. 8c). With increases in frequency as v_x , v_y , or v_{xy} , we observe the same trend as in the product-forming peaked topography (2P), result-

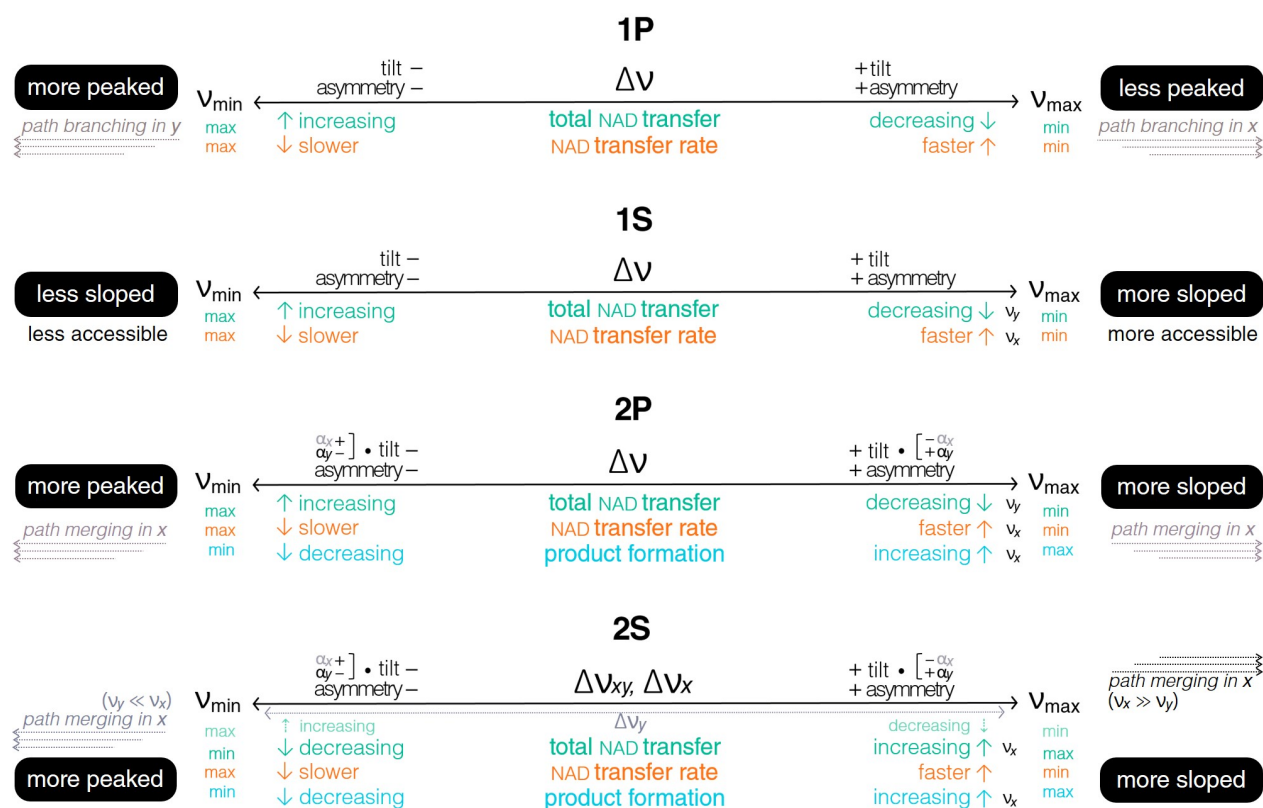


Fig. 9 General trends in the influence of Δv on conical intersection topography & photochemical observables of nonadiabatic transfer. In the 1P (peaked with one path), 1S (sloped with one path), 2P (peaked with two paths), and 2S (sloped with two paths) conical intersection models, modulation of the branching mode frequencies Δv (Δv_x , Δv_y , and Δv_{xy}) consistently influenced the total amount of nonadiabatic transfer to the ground state (total NAD transfer), the time required for completion of nonadiabatic transfer (NAD transfer rate), and the ground-state photoproduct yield (product formation). In cases where one frequency had a more significant influence on an observable, the dominant frequency (v_x or v_y) is labeled on the right side. Corresponding changes in key topographical parameters, tilt and cylindrical asymmetry, with Δv are indicated as an increase (+) or decrease (-). In cases where v_x and v_y had different effects on the tilt, they are labeled individually as the change in total tilt with Δv_x ($\pm\alpha_x$) versus with Δv_y ($\pm\alpha_y$). Black boxes summarize the effects of Δv on the overall peaked or sloped topographical character. Any tendencies toward the branching of one molecular pathway into two paths (in 1P, 1S) or merging of two paths into a single path (in 2P, 2S) along an axis, which would occur with Δv beyond v_{min}, v_{max} , are indicated (\Leftarrow, \Rightarrow).

ing in increasing photochemical quantum yields. This can again be attributed to greater v_x values that direct wavepacket momentum along the x -coordinate toward photoproduct formation, supported by greater v_y values that minimize the momentum used along the other coordinate—although in this model, momentum along the y -coordinate is still necessary to reach the conical intersection. Like in **2P**, v_x shows a greater influence on product yield than v_y , because x still corresponds to the reaction coordinate. Increasing v_x and v_y from 6–20 THz increased product formation from 18–42% (v_x), compared to 30–34% (v_y). One unique aspect of these results is that the product yield increases in parallel with the total nonadiabatic transfer (as v_x or v_{xy} increases). As also seen in the **2P** model, the branching frequencies have a more dramatic influence on the photoproduct yield than the total nonadiabatic transfer—and this dependence is preserved in **2S** even as the product yield increases *with* the amount of nonadiabatic transfer. This further illustrates the remarkable sensitivity of the photochemical process and its resulting product ratios to the precise topography of the conical intersection.

4.5 Summary

Overall, we observed that lower branching mode frequencies increase the extent of nonadiabatic transfer accomplished in both peaked and sloped conical intersections, due to a greater area of effective nonadiabatic coupling. Due to reduced wavepacket momentum during dynamics, however, more time is required for completion of nonadiabatic transfer with lower frequencies. In product-forming topographies **2P** and **2S**, the photochemical quantum yield showed an inverse response to vibrational frequency: higher frequencies elicit greater product yields, despite the simultaneous reduction in nonadiabatic transfer in most conditions. In all topographies, we observed coordinate-specific effects on nonadiabatic wavepacket dynamics and the resulting reaction properties. In general, topography along the reaction coordinate, x , showed a more prominent influence on the nonadiabatic transfer rate and the photoproduct yield, whereas topography along the y -coordinate demonstrated a greater influence on the total amount of nonadiabatic transfer. Because of these relationships, the sloped topography with two paths, **2S**, varied from the other cases due to the displacement of the conical intersec-

tion in y , which is absent in the other model topographies. Therefore we observed an opposite trend in the extent of nonadiabatic transfer in response to changes along the reaction coordinate or both coordinates. The prevailing trends (and any deviations) in the effects of Δv on specific topographical parameters, overall topography, and the primary photochemical observables measured from nonadiabatic transfer dynamics are summarized in Fig. 9.

5 Conclusions

In the models presented here, we have emphasized that the overall structure of potential energy surfaces and their conical intersection topographies enable them to serve different fundamental roles in photochemical processes and determine the pathways taken during excited-state decay. Furthermore, we have observed specific ways in which the precise topography of a conical intersection has far-ranging influences on the outcomes of excited-state processes, determining molecular properties that are standard references used throughout chemistry-related fields—such as photostability, photoreactivity, excited-state lifetime, reaction rate, and product yield. Specifically, we have demonstrated that modifying the vibrational mode frequencies alters both the overall curvature of the potential energy surfaces and the specific topography of the conical intersection. Our results show that these alterations can induce noticeable differences in fluorescence quantum yield and photoproduct quantum yield on the molecular scale, as well the rates of excited-state processes occurring on the ultrafast, electronic scale. Through simulations of vibrational wavepacket relaxation, this study provides detailed demonstration that the particular wavepacket and nonadiabatic transfer dynamics—which can vary dramatically with even minor topographical modifications—are responsible for the resulting photochemical properties.

We expect that the underlying principles and general relationships between topography, its effects on dynamics, and the resulting photochemistry quantified in this study will be applicable to further research in this field and others. Experimental techniques could be used to change the normal mode frequencies of a compound and modify its potential energy surface topography as a strategy for photochemical control¹³⁴—to induce formation of a specific product, or enhance the product yield or reaction rate, for example. This could be achieved through chemical modifications such as single-atom substitutions or functional group additions,^{29,44,121,122} or through isolation of specific molecular conformers.^{135,136} Other possible approaches also utilize the significance of vibrational modes in conical intersection-mediated processes by applying laser pulses to selectively activate relevant modes.^{36,122} Aside from vibrational modes, the potential energy surface topography can also be manipulated by exposing the sample to different conditions, such as pulsed lasers and electric fields,^{50–52,137–139} or even different solvents in some molecules.^{46,140–142} Overall, the results shown here present a framework for understanding—and modifying—conical intersection and potential energy surface topography, providing a basis for harnessing photochemical processes that take place through conical intersections in the future.

Conflicts of interest

There are no conflicts of interest to declare.

Acknowledgments

D.B.T. acknowledges support from the Alfred P. Sloan Foundation and from the National Science Foundation under CAREER Grant No. CHE-1552235. C.A.F. acknowledges support from the Margaret Strauss Kramer Fellowship. This work was supported in part through the NYU IT High Performance Computing resources, services, and staff expertise.

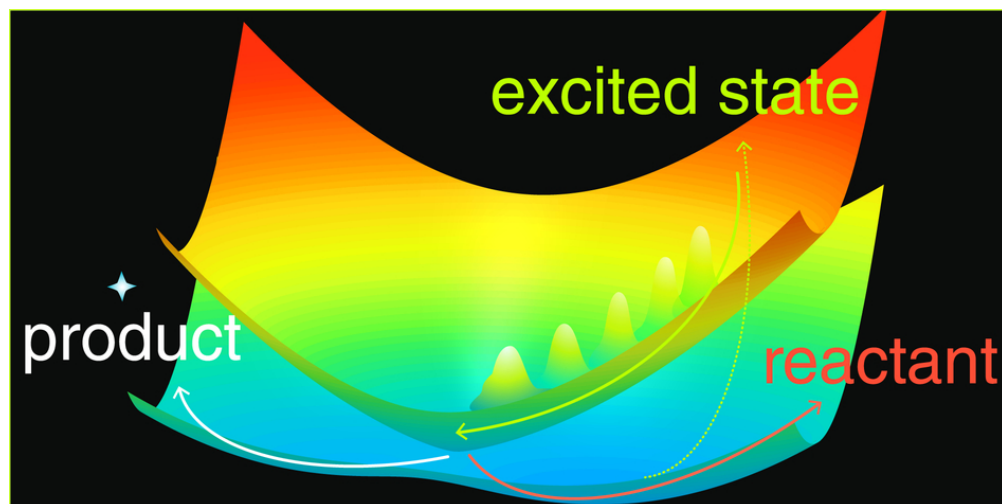
References

- 1 G. A. Worth and L. S. Cederbaum, *Annu. Rev. Phys. Chem.*, 2004, **55**, 127–158.
- 2 F. Bernardi, M. Olivucci and M. A. Robb, *Chem. Soc. Rev.*, 1996, **25**, 321–328.
- 3 D. R. Yarkony, *Rev. Mod. Phys.*, 1996, **68**, 985–1013.
- 4 S. Matsika and P. Krause, *Annu. Rev. Phys. Chem.*, 2011, **62**, 621–643.
- 5 M. S. Schuurman and A. Stolow, *Annu. Rev. Phys. Chem.*, 2018, **69**, 427–450.
- 6 K. Takatsuka, T. Yonehara, K. Hanasaki and Y. Arasaki, *Chemical Theory beyond the Born-Oppenheimer Paradigm: Nonadiabatic Electronic and Nuclear Dynamics in Chemical Reactions*, World Scientific Publishing, Singapore, 2014.
- 7 T. Yonehara, K. Hanasaki and K. Takatsuka, *Chem. Rev.*, 2012, **112**, 499–542.
- 8 S. Matsika, in *Reviews in Computational Chemistry*, ed. K. B. Lipkowitz, T. R. Cundari and D. B. Boyd, John Wiley & Sons, 2007, vol. 23, ch. 2. Conical Intersections in Molecular Systems, pp. 83–124.
- 9 M. A. Robb, F. Bernardi and M. Olivucci, *Pure & Appl. Chem.*, 1995, **67**, 783–789.
- 10 M. A. Robb, M. Garavelli, M. Olivucci and F. Bernardi, in *Reviews in Computational Chemistry*, ed. K. B. Lipkowitz and D. B. Boyd, John Wiley & Sons, 2007, vol. 15, ch. 2. A Computational Strategy for Organic Photochemistry, pp. 87–146.
- 11 W. T. Pollard, S.-Y. Lee and R. A. Mathies, *J. Chem. Phys.*, 1990, **92**, 4012–4029.
- 12 B. Lasorne, G. A. Worth and M. A. Robb, in *Molecular Quantum Dynamics: From Theory to Applications*, ed. F. Gatti, Springer-Verlag, 2014, ch. 7. Non-adiabatic Photochemistry: Ultrafast Electronic State Transitions and Nuclear Wavepacket Coherence, pp. 181–211.
- 13 J. Bazard, L. A. Bizimana, T. Gellen, W. P. Carbery and D. B. Turner, *J. Phys. Chem. Lett.*, 2016, **7**, 14–19.
- 14 K. Takatsuka and T. Yonehara, *Phys. Chem. Chem. Phys.*, 2011, **13**, 4987–5016.
- 15 J. Albert, K. Hader and V. Engel, *J. Chem. Phys.*, 2017, **147**, 064302.
- 16 K. Hader, J. Albert, E. K. U. Gross and V. Engel, *J. Chem. Phys.*, 2017, **146**, 074304.
- 17 B. F. E. Curchod and F. Agostini, *J. Phys. Chem. Lett.*, 2017, **8**, 831–847.

- 18 P. Hamm and G. Stock, *Phys. Rev. Lett.*, 2012, **109**, 173201.
- 19 B. Balzer, S. Hahn and G. Stock, *Chem. Phys. Lett.*, 2003, **379**, 351–358.
- 20 M. Erdmann, P. Marquetland and V. Engel, *J. Chem. Phys.*, 2003, **119**, 672–679.
- 21 S. Hahn and G. Stock, *J. Phys. Chem. B*, 2000, **104**, 1146–1149.
- 22 P. Cattaneo and M. Persico, *J. Phys. Chem. A*, 1997, **101**, 3454–3460.
- 23 S. Shin and H. Metiu, *J. Chem. Phys.*, 1995, **102**, 9285–9295.
- 24 G. J. Atchity, S. S. Xantheas and K. Ruedenberg, *J. Chem. Phys.*, 1991, **95**, 1862–1876.
- 25 D. R. Yarkony, *J. Chem. Phys.*, 2001, **114**, 2601–2613.
- 26 A. M. Virshup, J. Chen and T. J. Martínez, *J. Chem. Phys.*, 2012, **137**, 22A519.
- 27 P. Krause, S. Matsika, M. Kotur and T. Weinacht, *J. Chem. Phys.*, 2012, **137**, 22A537.
- 28 J. P. Malhado and J. T. Hynes, *J. Chem. Phys.*, 2016, **145**, 194104.
- 29 A. M. D. Lee, J. D. Coe, S. Ullrich, M.-L. Ho, S.-J. Lee, B.-M. Cheng, M. Z. Zgierski, I.-C. Chen, T. J. Martinez and A. Stolow, *J. Phys. Chem. A*, 2007, **111**, 11948–11960.
- 30 C. A. Farfan and D. B. Turner, *J. Phys. Chem. A*, 2019, **123**, 7768–7776.
- 31 D.-L. Qi, D. Hong-Guang, Z.-R. Sun, R. J. D. Miller and M. Thorwart, *J. Chem. Phys.*, 2017, **147**, 074101.
- 32 H.-G. Duan, R. J. D. Miller and M. Thorwart, *J. Phys. Chem. Lett.*, 2016, **7**, 3491–3496.
- 33 A. Sanchez-Galvez, P. Hunt, M. A. Robb, M. Olivucci, T. Vreven and H. B. Schlegel, *J. Am. Chem. Soc.*, 2000, **122**, 2911–2924.
- 34 M. Ben-Nun, F. Molnar, K. Schulten and T. J. Martínez, *Proc. Natl. Acad. Sci. U.S.A.*, 2002, **99**, 1769–1773.
- 35 J. Quenneville and T. J. Martínez, *J. Phys. Chem. A*, 2003, **107**, 829–837.
- 36 B. Lasorne, M. J. Bearpark, M. A. Robb and G. A. Worth, *J. Phys. Chem. A*, 2008, **112**, 13017–13027.
- 37 D. Asturiol, B. Lasorne, G. A. Worth, M. A. Robb and L. Blancafort, *Phys. Chem. Chem. Phys.*, 2010, **12**, 4949–4958.
- 38 B. Dietzek, B. Brüggemann, T. Pascher and A. Yartzev, *Phys. Rev. Lett.*, 2006, **97**, 258301.
- 39 E. Riedle, M. K. Roos, S. Thallmair, C. F. Sailer, N. Krebs, B. P. Fingerhut and R. de Vivie-Riedle, *Chem. Phys. Lett.*, 2017, **683**, 128–134.
- 40 W. Fuß, S. Lochbrunner, A. M. Müller, T. Schikarski, W. E. Schmid and S. A. Trushin, *Chem. Phys.*, 1998, **232**, 161–174.
- 41 M. A. Robb and M. Olivucci, *J. Photochem. Photobiol., A*, 2001, **5737**, 1–7.
- 42 S. Matsika, C. Zhou, M. Kotur and T. C. Weinacht, *Faraday Discuss.*, 2011, **153**, 247–260.
- 43 M. Sukharev and T. Seideman, *Phys. Rev. A*, 2005, **71**, 012509.
- 44 H. Ichikawa and K. Takatsuka, *J. Phys. Chem. A*, 2017, **121**, 315–325.
- 45 D. Mendive-Tapia, B. Lasorne, G. A. Worth, M. J. Bearpark and M. A. Robb, *Phys. Chem. Chem. Phys.*, 2010, **48**, 15725–15733.
- 46 A. Kahan, A. Wand, S. Ruhman, S. Zilberg and Y. Haas, *J. Phys. Chem. A*, 2011, **115**, 10854–10861.
- 47 S. Scheit, Y. Arasaki and K. Takatsuka, *J. Phys. Chem. A*, 2012, **116**, 2644–2653.
- 48 M. Olivucci and F. Santoro, *Angew. Chem. Int. Ed.*, 2008, **47**, 6322–6325.
- 49 T. Rozgonyi and L. González, *Chem. Phys. Lett.*, 2008, **459**, 39–43.
- 50 X. F. Xu, A. Kahan, S. Zilberg and Y. Haas, *J. Phys. Chem. A*, 2009, **113**, 9779–9791.
- 51 Y. Arasaki and K. Takatsuka, *Phys. Chem. Chem. Phys.*, 2010, **12**, 1239–1242.
- 52 M. Richter, F. Bouakline, J. González-Vázquez, L. Martínez-Fernández, I. Corral, S. Patchkovskii, F. Morales, M. Y. Ivanov, F. Martín and O. Smirnova, *New J. Phys.*, 2015, **17**, 113023.
- 53 D. R. Yarkony, *J. Phys. Chem. A*, 2001, **105**, 6277–6293.
- 54 I. F. Galván, M. G. Delcey, T. B. Pedersen, F. Aquilante and R. Lindh, *J. Chem. Theor. Comput.*, 2016, **12**, 3636–3653.
- 55 S. Ullrich, T. Schultz, M. Z. Zgierski and A. Stolow, *Phys. Chem. Chem. Phys.*, 2004, **6**, 2796–2801.
- 56 H. R. Hudock, B. G. Levine, A. L. Thompson, H. Satzger, D. Townsend, N. Gador, S. Ullrich, A. Stolow and T. J. Martínez, *J. Phys. Chem. A*, 2007, **111**, 8500–8508.
- 57 S. Hayashi, E. Tajkhorshid and K. Schulten, *Biophys. J.*, 2009, **96**, 403–416.
- 58 D. Polli, P. Altoe, O. Weingart, K. M. Spillane, C. Manzoni, D. Brida, G. Tomasello, G. Orlandi, P. Kukura, R. A. Mathies, M. Garavelli and G. Cerullo, *Nature*, 2010, **467**, 440–443.
- 59 P. J. M. Johnson, M. H. Farag, A. Halpin, T. Morizumi, V. I. Prokhorenko, J. Knoester, T. L. C. Jansen, O. P. Ernst and R. J. D. Miller, *J. Phys. Chem. B*, 2017, **121**, 4040–4047.
- 60 J. Serrano-Pérez, F. de Vleeschouwer, F. de Proft, D. Mendive-Tapia, M. J. Bearpark and M. A. Robb, *J. Org. Chem.*, 2013, **78**, 1874–1886.
- 61 I. J. Palmer, I. N. Ragazos, F. Bernardi, M. Olivucci and M. A. Robb, *J. Am. Chem. Soc.*, 1993, **115**, 673–682.
- 62 M. Garavelli, F. Bernardi, M. Olivucci, M. J. Bearpark, S. Klein and M. A. Robb, *J. Phys. Chem. A*, 2001, **105**, 11496–11504.
- 63 P. Celani, S. Ottani, M. Olivucci, F. Bernardi and M. A. Robb, *J. Am. Chem. Soc.*, 1994, **116**, 10141–10151.
- 64 A. Nenov, W. J. Schreier, F. O. Koller, M. Braun, R. de Vivie-Riedle, W. Zinth and I. Pugliesi, *J. Phys. Chem. A*, 2012, **116**, 10518–10528.
- 65 I. Schapiro, M. N. Ryazantsev, L. M. Frutos, N. Ferré, R. Lindh and M. Olivucci, *J. Am. Chem. Soc.*, 2011, **133**, 3354–3364.
- 66 M. Garavelli, P. Celani, F. Bernardi, M. A. Robb and M. Olivucci, *J. Am. Chem. Soc.*, 1997, **119**, 6891–6901.
- 67 J. Ghosh, S. Bhaumik and A. Bhattacharya, *Chem. Phys.*, 2018, **513**, 221–229.

- 68 B. Sellner, M. Ruckebauer, I. Stambolić, M. Barbatti, A. J. A. Aquino and H. Lischka, *J. Phys. Chem. A*, 2010, **114**, 8778–8785.
- 69 A.-H. Gao, B. Li, P.-Y. Zhang and J. Liu, *Comput. Theor. Chem.*, 2014, **1031**, 13–21.
- 70 C. R. Crecca and A. E. Roitberg, *J. Phys. Chem. A*, 2006, **110**, 8188–8203.
- 71 S. Gozem, H. L. Luk, I. Schapiro and M. Olivucci, *Chem. Rev.*, 2017, **117**, 13502–13565.
- 72 S. Gozem, F. Melaccio, R. Lindh, A. I. Krylov, A. A. Granovsky, C. Angeli and M. Olivucci, *J. Chem. Theory Comput.*, 2013, **9**, 4495–4506.
- 73 Y. Amatatsu and Y. Komura, *J. Chem. Phys.*, 2006, **125**, 174311.
- 74 M. J. Bearpark, F. Bernardi, S. Clifford, M. Olivucci, M. A. Robb, B. R. Smith and T. Vreven, *J. Am. Chem. Soc.*, 1996, **118**, 169–175.
- 75 J. Segarra-Martí, T. Tran and M. J. Bearpark, *Phys. Chem. Chem. Phys.*, 2019, **21**, 14322–14330.
- 76 M. Merchán, R. González-Luque, T. Climent, L. Serrano-Andrés, E. Rodríguez, M. Reguero and D. Peláez, *J. Phys. Chem. B*, 2006, **110**, 26471–26476.
- 77 N. Ismail, L. Blancafort, M. Olivucci, B. Kohler and M. A. Robb, *J. Am. Chem. Soc.*, 2002, **124**, 6818–6819.
- 78 A. L. Sobolewski and W. Domcke, *Eur. Phys. J. D*, 2002, **20**, 369–374.
- 79 N. Bellonzi, E. Alguire, S. Fatehi, Y. Shao and J. E. Subotnik, *J. Chem. Phys.*, 2020, **152**, 044112.
- 80 H.-H. Teh and J. E. Subotnik, *J. Phys. Chem. Lett.*, 2019, **10**, 3426–3432.
- 81 W.-K. Chen, X.-Y. Liu, W.-H. Fang, P. O. Dral and G. Cui, *J. Phys. Chem. Lett.*, 2018, **9**, 6702–6708.
- 82 D. Hollas, L. Šišťík, E. G. Hohenstein, T. J. Martínez and P. Slavíček, *J. Chem. Theory Comput.*, 2018, **14**, 339–350.
- 83 B. S. Fales, Y. Shu, B. G. Levine and E. G. Hohenstein, *J. Chem. Phys.*, 2017, **147**, 094104.
- 84 B. F. E. Curchod and T. J. Martínez, *Chem. Rev.*, 2018, **118**, 3305–3336.
- 85 M. P. Bircher, E. Liberatore, N. J. Browning, S. Brickel, C. Hofmann, A. Patoz, O. T. Unke, T. Zimmermann, M. Chergui, P. Hamm, U. Keller, M. Meuwly, H.-J. Werner, J. Vaníček and U. Rothlisberger, *Struct. Dyn.*, 2017, **4**, 061510.
- 86 H. Guo and D. R. Yarkony, *Phys. Chem. Chem. Phys.*, 2016, **18**, 26335–26352.
- 87 J. P. Malhado, M. J. Bearpark and J. T. Hynes, *Front. Chem.*, 2014, **2**, 97.
- 88 T. Yonehara, S. Takahashi and K. Takatsuka, *J. Chem. Phys.*, 2009, **130**, 214113.
- 89 D. R. Yarkony, *Acc. Chem. Res.*, 1998, **31**, 511–518.
- 90 R. G. Mckinlay, J. M. Žurek and M. J. Paterson, in *Theoretical and Computational Inorganic Chemistry*, ed. R. van Eldik and J. Harvey, Academic Press, 2010, vol. 62, ch. 9. Vibronic Coupling In Inorganic Systems: Photochemistry, Conical Intersections, And The Jahn–Teller And Pseudo-Jahn–Teller Effects, pp. 351–390.
- 91 I. B. Bersuker, *Chem. Rev.*, 2001, **101**, 1067–1114.
- 92 D. G. Truhlar and C. A. Mead, *Phys. Rev. A*, 2003, **68**, 032501.
- 93 M. Erdmann, S. Baumann, S. Gräfe and V. Engel, *Eur Phys J D*, 2004, **30**, 327–333.
- 94 A. Ferretti, G. Granucci, A. Lami, M. Persico and G. Villani, *J. Chem. Phys.*, 1996, **104**, 5517–5527.
- 95 U. Manthe and H. Köppel, *J. Chem. Phys.*, 1990, **93**, 345–356.
- 96 R. Chávez-Calvillo and J. Hernández-Trujillo, *J. Phys. Chem. A*, 2011, **115**, 13036–13044.
- 97 S. Sardar, P. Puzari and S. Adhikari, *Phys. Chem. Chem. Phys.*, 2011, **13**, 15960–15972.
- 98 J. R. Fair, D. Schaefer, R. Kosloff and D. J. Nesbitt, *J. Chem. Phys.*, 2002, **116**, 1406–1416.
- 99 J. C. Light, I. P. Hamilton and J. V. Lill, *J. Chem. Phys.*, 1985, **82**, 1400–1409.
- 100 P. F. Endres, *J. Chem. Phys.*, 1967, **47**, 798–799.
- 101 D. O. Harris, G. G. Engerholm and W. D. Gwinn, *J. Chem. Phys.*, 1965, **43**, 1515–1517.
- 102 E. Camrud and D. B. Turner, *J. Chem. Ed.*, 2017, **94**, 582–591.
- 103 R. G. Littlejohn, M. Cargo, T. Carrington Jr., K. A. Mitchell and B. Poirier, *J. Chem. Phys.*, 2002, **116**, 8691–8703.
- 104 R. Kosloff, *J. Phys. Chem.*, 1988, **92**, 2087–2100.
- 105 M. M. T. El-Tahawy, A. Nenov, O. Weingart, M. Olivucci and M. Garavelli, *J. Phys. Chem. Lett.*, 2018, **9**, 3315–3322.
- 106 C. Schnedermann, X. Yang, M. Liebel, K. Spillane, J. Lugtenburg, I. Fernandez, A. Valentini, I. Schapiro, M. Olivucci, P. Kukura and R. A. Mathies, *Nature Chemistry*, 2018, **10**, 449–455.
- 107 S. L. Li and D. G. Truhlar, *J. Chem. Phys.*, 2017, **146**, 064301.
- 108 M. Boggio-Pasqua, M. Ravaglia, M. J. Bearpark, M. Garavelli and M. A. Robb, *J. Phys. Chem. A*, 2003, **107**, 11139–11152.
- 109 F. Sicilia, L. Blancafort, M. J. Bearpark and M. A. Robb, *J. Phys. Chem. A*, 2007, **111**, 2182–2192.
- 110 A. Migani, A. Sinicropi, N. Ferré, A. Cembran, M. Garavelli and M. Olivucci, *Faraday Discuss.*, 2004, **127**, 179–191.
- 111 A. Migani, M. A. Robb and M. Olivucci, *J. Am. Chem. Soc.*, 2003, **125**, 2804–2808.
- 112 J. Casellas, M. J. Bearpark and M. Reguero, *Chem. Phys. Chem.*, 2016, **17**, 3068–3079.
- 113 Q. Li, D. Mendive-Tapia, M. J. Paterson, A. Migani, M. J. Bearpark, M. A. Robb and L. Blancafort, *Chem. Phys.*, 2010, **377**, 60–65.
- 114 A. Nenov, P. Kölle, M. A. Robb and R. de Vivie-Riedle, *J. Org. Chem.*, 2010, **75**, 123–129.
- 115 M. Boggio-Pasqua, M. J. Bearpark, F. Ogliaro and M. A. Robb, *J. Am. Chem. Soc.*, 2006, **128**, 10533–10540.
- 116 M. Boggio-Pasqua, M. J. Bearpark, P. A. Hunt and M. A. Robb, *J. Am. Chem. Soc.*, 2002, **124**, 1456–1470.
- 117 M. Ben-Nun, J. Quenneville and T. J. Martínez, *J. Phys.*

- Chem. A*, 2000, **104**, 5161–5175.
- 118 E. Marsili, M. H. Farag, X. Yang, L. De Vico and M. Olivucci, *J. Phys. Chem. A*, 2019, **123**, 1710–1719.
- 119 M. Manathunga, X. Yang, H. L. Luk, S. Gozem, L. M. Frutos, A. Valentini, N. Ferrè and M. Olivucci, *J. Chem. Theory Comput.*, 2016, **12**, 839–850.
- 120 T. van Voorhis, T. Kowalczyk, B. Kaduk, L.-P. Wang, C.-L. Cheng and Q. Wu, *Annu. Rev. Phys. Chem.*, 2010, **61**, 149–170.
- 121 S. P. Neville, Y. Wang, A. E. Boguslavskiy, A. Stolow and M. S. Schuurman, *J. Chem. Phys.*, 2016, **144**, 014305.
- 122 J. S. Lim, Y. S. Lee and S. K. Kim, *Angew. Chem. Int. Ed.*, 2008, **47**, 1853–1856.
- 123 M. Falge, V. Engel and S. Gräfe, *J. Chem. Phys.*, 2011, **134**, 184307.
- 124 B. F. E. Curchod, I. Tavernelli and U. Rothlisberger, *Phys. Chem. Chem. Phys.*, 2011, **13**, 3231–3236.
- 125 I. G. Ryabinkin, L. Joubert-Doriol and A. F. Izmaylov, *Acc. Chem. Res.*, 2017, **50**, 1785–1793.
- 126 L. Joubert-Doriol, J. Sivasubramanium, I. G. Ryabinkin and A. F. Izmaylov, *J. Phys. Chem. Lett.*, 2017, **8**, 452–456.
- 127 L. Joubert-Doriol, I. G. Ryabinkin and A. F. Izmaylov, *J. Chem. Phys.*, 2013, **139**, 234103.
- 128 A. K. Belyaev, C. Lasser and G. Trigila, *J. Chem. Phys.*, 2014, **140**, 224108.
- 129 S. Nanbu, T. Ishida and H. Nakamura, *Chem. Sci.*, 2010, **1**, 663–674.
- 130 H. Köppel, in *Quantum Dynamics of Complex Molecular Systems*, ed. D. A. Micha and I. Burghardt, Springer, 2007, ch. 5. Nonadiabatic Multimode Dynamics at Symmetry-Allowed Conical Intersections, pp. 113–133.
- 131 S. Mahapatra and H. Köppel, *J. Chem. Phys.*, 1998, **109**, 1721–1733.
- 132 G. G. Kochendoerfer and R. A. Mathies, *J. Phys. Chem.*, 1996, **100**, 14526–14532.
- 133 P. J. M. Johnson, A. Halpin, T. Morizumi, V. I. Prokhorenko, O. P. Ernst and R. J. D. Miller, *Nature Chemistry*, 2015, **7**, 980–986.
- 134 A. H. Zewail, *Femtochemistry: Ultrafast Dynamics of the Chemical Bond*, World Scientific, 1994.
- 135 M. H. Kim, L. Shen, H. Tao, T. J. Martinez and A. G. Suits, *Science*, 2007, **315**, 1561–1565.
- 136 S. T. Park, S. K. Kim and M. S. Kim, *Nature*, 2002, **415**, 306–308.
- 137 Y. Arasaki, Y. Mizuno, S. Scheit and K. Takatsuka, *J. Chem. Phys.*, 2016, **144**, 044107.
- 138 S. Scheit, Y. Arasaki and K. Takatsuka, *J. Chem. Phys.*, 2014, **140**, 244115.
- 139 B. J. Sussman, M. Y. Ivanov and A. Stolow, *Phys. Rev. A*, 2005, **71**, 051401(R).
- 140 S. Alfalah, S. Zilberg and Y. Haas, *Chem. Phys. Lett.*, 2008, **459**, 100–104.
- 141 J. Voll, T. Kerscher, D. Geppert and R. de Vivie-Riedle, *J. Photochem. Photobiol., A*, 2007, **190**, 352–358.
- 142 F. Santoro, V. Barone, T. Gustavsson and R. Improta, *J. Am. Chem. Soc.*, 2006, **128**, 16312–16322.



80x40mm (300 x 300 DPI)